Copyright © 2014 Tech Science Press CMES, vol.97, no.3, pp.239-279, 2014

A State Space Differential Reproducing Kernel Method for the Buckling Analysis of Carbon Nanotube-Reinforced Composite Circular Hollow Cylinders

Chih-Ping Wu[1,2] **and Ruei-Yong Jiang**[1]

Abstract: A state space differential reproducing kernel (DRK) method is developed for the three-dimensional (3D) buckling analysis of simply-supported, carbon nanotube-reinforced composite (CNTRC) circular hollow cylinders and laminated composite ones under axial compression. The single-walled carbon nanotubes (CNTs) and polymer are used as the reinforcements and matrix, respectively, to constitute the CNTRC cylinder. Three different distributions of CNTs varying in the thickness direction are considered (i.e., the uniform distribution and functionally graded rhombus-, and X-type ones), and the through-thickness distributions of effective material properties of the cylinder are determined using the rule of mixtures. The 3D linear buckling theory is used, in which a set of membrane stresses is assumed to exist in the cylinder just before instability occurs, and this is regarded as the initial stresses introduced in the formulation. The Euler-Lagrange equations perturbed from the state of neutral equilibrium are derived using the Reissner mixed variational theorem. The primary field variables, displacement and transverse stress components, are expanded as the single Fourier series in the circumferential coordinate, and then interpolated in the axial coordinate using DRK interpolation functions. Finally, the state space equations of this problem are obtained, which represent a system of ordinary differential equations in the thickness coordinate. The state space DRK solutions of the critical load parameters of the cylinder can thus be obtained by means of the transfer matrix method combined with the successive approximation one, and the convergence and accuracy of the state space DRK solutions are validated by comparing these solutions with exact 3D ones available in the literature and approximate 3D ones obtained using the ANSYS software.

Keywords: Meshless methods, state space methods, buckling, functionally graded materials, Carbon nanotubes, Cylinders.

[1] Department of Civil Engineering, National Cheng Kung University, Tainan 70101, Taiwan, ROC.
[2] Corresponding author. Email: cpwu@mail.ncku.edu.tw

1 Introduction

The stability of functionally graded material (FGM) structures is an important subject in various engineering applications because it is the dominant failure occurring in these structures, and has therefore attracted considerable attention in recent decades. Unlike the conventional fiber-reinforced composite (FRC) structures, such as the graphite/epoxy, boron/epoxy and glass/epoxy composite ones, the material properties of which are layer-wise constant variations through the thickness direction, those of FGM structures are designed to vary continuously and smoothly through this, which results in a more complicated problem to be analyzed than that involving FRC structures.

Carbon nanotubes (CNTs) have extraordinary mechanical properties, and have thus started to be used as reinforcements, instead of conventionally continuous carbon (graphite) fibers, that are randomly embedded in the polymer matrix to produce carbon nanotube-reinforced composite (CNTRC) structures [Coleman et al. (2006); Esawi and Farag (2007); Chou et al. (2010)]. Various mechanical analyses of these structures are thus needed to realize their static and dynamic characteristics, the results of which can be used to provide design standards to engineers, and enhance the lifetimes of the related objects. Comprehensive surveys with regard to the relevant theoretical methodologies and numerical models of FRC/CNTRC structures can be found in the literature [Noor and Burton (1990a, b, 1996); Noor et al. (1991); Saravanos and Heyliger (1999); Odegard et al. (2002); Carrera (2000a, b, 2003); Wu et al. (2008); Carrera and Brischetto (2009); Hackett and Bennett (2012)]. Among these articles, the current literature survey will focus on those ones dealing with the buckling and postbuckling analyses of functionally graded (FG) CNTRC cylinders and laminated FRC ones under thermo-mechanical loads.

Numerous two-dimensional (2D) buckling analyses of FG CNTRC cylinders and laminated FRC ones subjected to thermo-mechanical loads have been presented. Sallam and Simitses (1987) and Simitses and Chen (1988) studied the delamination buckling of cylindrical shells with either fully simply-supported or clamped edges and under external pressure and axial compression, in which Donnell-type kinematic nonlinearity [Donnell (1976)] and linearly elastic material behavior were used. Based on higher-order shear deformation theory (HSDT), Anastasiadis and Simitses (1993) presented the buckling analysis of pressure-loaded, laminated cylindrical shells, in which the buckling equations corresponding to the classical shell theory (CST), first-order shear deformation theory (FSDT), and HSDT were derived, and their results were compared with those of other work. Anastasiadis et al. (1994) presented the instability behaviors of moderately thick, laminated cylindrical shells under combined axial compression and external pressure, in which a parametric study with regard to the effects of those on the critical load parameter-

s of the shells was carried out, such as the effects of shear deformation, stacking sequence, and length-to-radius and radius-to-thickness ratios. Dumir et al. (2001, 2003, 2005) presented the axisymmetric static and dynamic buckling of laminated, moderately thick truncated conical caps and annular spherical ones with combinations of clamped and simply-supported edges and under transverse loads, in which the Marguerre-type FSDT was formulated, and the dependence of the transverse shear deformation effect on the thickness parameter for various boundary conditions was investigated. Based on the HSDT combined with von Karman kinematic nonlinearity, Shen and Chen (1991), Shen et al. (1991) and Shen (2001) undertook the buckling and postbuckling analyses of stiffened and non-stiffened laminated cylindrical shells under hygrothermal environments, and combined axial compression and external pressure. Shen (2011a, b, 2012) also presented the analyses of CNTRC cylindrical shells under pure axial compression and pure external pressure in thermal environments, in which the material properties were considered to be temperature-dependent and assumed to be either uniformly distributed (UD) or varying in functionally graded manner through the thickness coordinate. Lei et al. (2013a, b) developed the element-free *kp*-Ritz method for the nonlinear bending and linear buckling analyses of CNTRC plates under various in-plane mechanical loads, the material properties of which were estimated using either the Eshelby-Mori-Tanaka approach or the extended rule of mixtures. The results demonstrated that the effects of the volume fraction of CNTs, different distributions of CNTs, aspect ratio, length-to-thickness ratio and different loading conditions on critical load parameters of the plate are significant.

While some exact and approximate three-dimensional (3D) buckling analyses of laminated composite structures and FGM ones have also been presented, such analyses are relatively few in comparison with the above-mentioned 2D ones, because they require more mathematical manipulation. Kardomateas (1993, 1995) presented the 3D buckling analysis of thick orthotropic circular hollow cylinders under axial compression and external pressure, in which the bifurcation of equilibrium of these cylinders was studied on the basis of 3D elasticity theory, and the critical loads over a wide range of the length-to-radius and thickness-to-radius ratios were discussed. Based on the principle of virtual displacements (PVD), Soldatos and Ye (1994) and Ye and Soldatos (1995) developed the state space method in combination with the successive approximation (SA) one to study the 3D buckling of homogeneous/laminated composite cylinders and cylindrical panels. Within the framework of 3D elasticity theory, Wu and Chen (2001) presented asymptotic solutions for the buckling of multilayered anisotropic conical shells under axial compression, in which the 3D axially compressed buckling problem was separated into a series of 2D buckling ones governing with the partially differential equations of

the CST, and the differential quadrature (DQ) method was used to determine the critical load parameter of each order problem, which can then be obtained order-by-order in a consistent and hierarchical manner. This 3D asymptotic approach was subsequently extended to the thermoelastic buckling and thermally induced dynamic instability of laminated composite conical shells by Wu and Chiu (2001, 2002). Based on Carrera's unified formulation (CUF) [Carrera (2003); Carrera and Ciuffreda (2005)] combined with a variable kinematics model, Carrera and Soave (2011) and D'Ottavio and Carrera (2010) carried out the linear buckling analyses of FGM structures and laminated composite ones. It is noted that most of the above-mentioned articles deal with the 3D buckling analysis of laminated FRC plates/shells, and few examine FG CNTRC structures.

The state space method [Ye (2003)] has been successfully used for exact 3D vibration, buckling and bending analyses of simply-supported, laminated FRC plates/shells and FGM ones by Ye and Soldatos (1994a, b), Chen et al. (2001), and Wu and Liu (2007). In recent years, this method has been used in combination with other numerical modeling approaches to undertake the analyses of structures with various boundary conditions. For example, Sheng and Ye (2002, 2003) developed a 3D state space finite element method (FEM) for the static analysis of laminated composite plates and cylindrical shells, in which the traditional FEM was used to approximate the in-surface variations of state variables, and a state space formulation was then obtained to determine the through-thickness distributions of assorted field variables. This state space FEM was also extended to investigate the free-edge effect on the bending and extensional analyses of cross-ply laminated hollow cylinders subjected to transverse and in-surface mechanical loads by Ye and Sheng (2003) and Ye et al. (2004). Chen and Lü (2005) and Lü et al. (2008, 2009) developed a state space DQ method for the approximate 3D bending analysis of laminated composite plates and FGM ones with one pair of simply supported opposite edges, in which the DQ method, instead of the FEM, was used to interpolate the primary variables.

In recent decades, a new class of computational methods, so-called meshless methods, have been developed and applied to a variety of mechanical problems with elastic solids, in which the construction of the shape functions of the unknown function is based on a set of randomly distributed nodes without any predefined mesh to provide connectivity of the nodes, unlike the conventional FEMs, in which this is based on a predefined one. In these meshless methods, the unknown approximation and interpolation are constructed using the moving least squares, reproducing kernel, and radial basis function schemes. Comprehensive surveys of meshless methods have been undertaken by Belytschko et al. (1996), Atluri and Shen (2002a, b), Atluri (2004), Li and Liu (2002, 2004), Liu and Gu (2005) and

Liew et al. (2011). In this paper, the literature survey will focus on the mechanical analysis of FGM structures using the meshless methods. Based on the Reissner-Mindlin theory, Sladek et al. (2008a, b) presented the elasto-thermal analyses of FGM plates and shallow shells under thermal loading and using the meshless local Petrov-Galerkin (MLPG) method, which has also been used for the stress, displacement and heat conduction analyses of 3D anisotropic FG solids [Sladek et al. (2008, 2009)]. Based on the FSDT, Zhao et al. (2009a, b) and Zhao and Liew (2011) developed an element-free *kp*-Ritz method for the thermo-elastic and free vibration analyses of FG plates, cylindrical shells and conical ones. The meshless methods not only provide a novel alternative for the mechanical analyses of FG elastic and piezoelectric structures and laminated FRC ones, but also overcome some drawbacks of FEM with regard to treating discontinuity, moving boundary and large deformation problems.

The differential reproducing kernel (DRK) interpolation method and its Hermite counterparts [Yang et al. (2010); Wang et al. (2010); Chen et al. (2011)] were developed for the analysis of elastic solids, in which the determination of shape functions of derivatives of RK interpolation functions were obtained using a set of differential reproducing conditions without taking the differentiation from the RK ones, which makes these DRK methods less time-consuming and more efficient for the calculation of the derivatives of unknown functions. Based on the above-mentioned benefits of the state space and DRK interpolation methods, Wu and Jiang (2012) proposed a state space DRK method to investigate the 3D static behaviors of sandwiched FGM/FRCM hollow circular cylinders with combinations of simply-supported and clamped edges and under transverse mechanical loads, which were also studied by Wu and Li (2013) using the finite cylindrical prism method based on the Reissner mixed variational theorem (RMVT) [Reissner (1984, 1986)], which is an extension of the finite cylindrical layer method developed by Wu and Chang (2012) for the approximate 3D analysis of simply supported, FGM sandwich cylinders.

After a close literature survey, we found that there are few articles dealing with the 3D axially compressed buckling analysis of multilayered FGM cylinders, very few that deal with CNTRC ones, and that state space-based numerical models seem to be an efficient tool for the analysis of functionally graded CNTRC structures and laminated FRC ones. This article thus aims at applying the state space DRK method, in which the DRK interpolation functions, proposed by Wang et al. (2010) and Wu and Yang (2011a, b), is used to interpolate the primary field variables. Based on 3D linear buckling theory, in which a set of membrane stresses is assumed to exist in the cylinder just before instability occurs, and which are introduced as the initial ones in the formulation, we derive the Euler-Lagrange equations perturbed

from the state of neutral equilibrium using the RMVT, the advantages of which have been stated by Wu and Tsai (2012) and Wu and Jiang (2011). The solution process of this state space DRK method is described as follows: (a) the primary field variables are first expanded as the single Fourier series in the circumferential coordinate, and then the 3D problem can be reduced to a 2D one; (b) these variables are further interpolated in the axial coordinate using DRK interpolation functions, with which the corresponding boundary conditions are required to be satisfied; (c) the state space equations of this 3D buckling problem are obtained, which represent a system of ordinary differential equations in the thickness coordinate, and the state space DRK solutions can then be obtained by means of the transfer matrix method combined with the SA one. In the illustrative examples, the accuracy and convergence of this method are examined by comparing these solutions with the exact 3D ones of simply-supported, multilayered composite cylinders available in the literature as well as with the accurate solutions of those cylinders using the ANSYS software. Moreover, a parametric study with regard to some geometric and material parameter effects on the critical load parameters of FG CNTRC cylinders and laminated FRC ones is carried out, such as the volume fraction of CNTs, different distributions of CNTs, and radius-to-thickness and length-to-radius ratios.

2 Carbon nanotube-reinforced composite cylinders

In this article, we consider either a carbon nanotube-reinforced cylinder or a laminated FRC one, as shown in Fig. 1, in which the edges of the cylinder are simply supported, and L, R and h denote the length, mid-surface radius and thickness of the cylinder, respectively. The global cylindrical coordinates (i.e., x, θ and r ones) are located on the center of the cylinder, and the global and local thickness coordinates (i.e., ζ and z_m $(m = 1 - N_l)$ ones, in which N_l is the total number of the layers constituting the cylinder) are located on the mid-surface of the cylinder and that of each layer, respectively, in which, $r = R + \zeta$, and $\zeta = [(\zeta_m + \zeta_{m-1})/2] + z_m$, where ζ_m and ζ_{m-1} are the thickness coordinates of the top and bottom surfaces of the m^{th}-layer. The thicknesses of each individual layer and the cylinder are h_m $(m = 1, 2, \cdots, N_l)$ and h, respectively, while $\sum_{m=1}^{N_l} h_m = h$.

There are three different distribution functions of carbon nanotubes varying in the thickness direction considered in this article, which are the uniform distribution (UD) function, and FG rhombus- (R-), and X-shaped ones. The rule of mixtures is used to determine the through-thickness distributions of effective material properties of the CNTRC cylinder, which are written as follows:

$$E_{11} = \eta_1 V_{CNT} (E_{11})_{CNT} + (V_m E_m), \tag{1a}$$

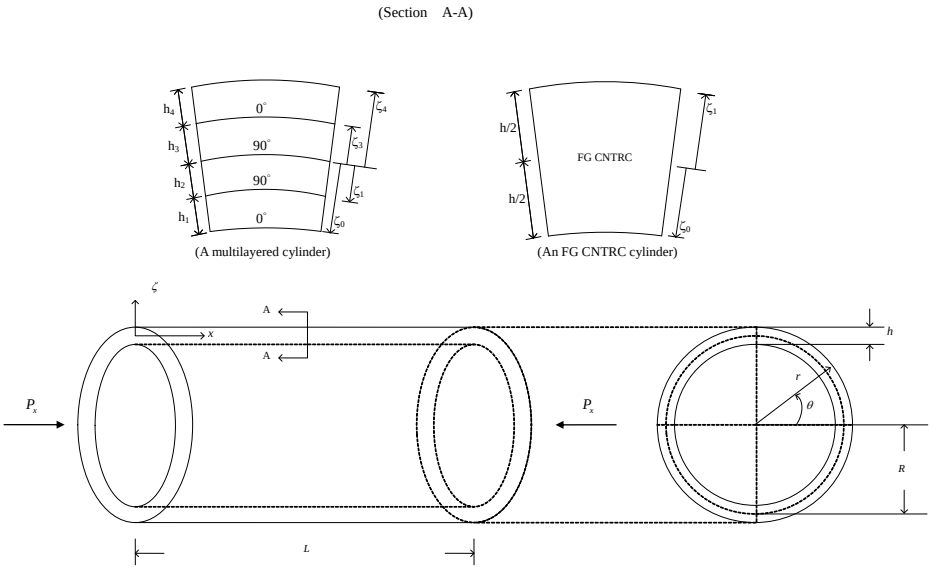

Figure 1: The configuration and coordinates of an FG CNTRC cylinder and a laminated composite one.

$$(\eta_2/E_{22}) = V_{CNT}/\left(E_{22}\right)_{CNT} + (V_m/E_m), \tag{1b}$$

$$(\eta_3/G_{12}) = V_{CNT}/\left(G_{12}\right)_{CNT} + (V_m/G_m), \tag{1c}$$

in which $(E_{11})_{CNT}$, $(E_{22})_{CNT}$, and $(G_{12})_{CNT}$ denote the Young's moduli and shear modulus of CNTs; E_m and G_m stand for those of the polymer; η_i $(i = 1, 2, 3)$ are the CNT efficiency parameters, and V_{CNT} and V_m are the volume fractions of CNTs and polymer, respectively, in which $V_{CNT} + V_m = 1$.

The through-thickness distributions of the volume fraction of CNTs, V_{CNT}, for the above-mentioned three types of CNTRC cylinders are given as follows:

$$V_{CNT} = V^*_{CNT}, \qquad \text{(UD-type CNTRC cylinders)}, \tag{2a}$$

$$V_{CNT}(\zeta) = 2\left[1 - (2|\zeta|/h)\right] V^*_{CNT} \quad \text{(FG R-type CNTRC cylinders)}, \tag{2b}$$

$$V_{CNT}(\zeta) = 2\,(2|\zeta|/h)\; V^*_{CNT} \qquad \text{(FG X-type CNTRC cylinders)}, \tag{2c}$$

in which

$$V^*_{CNT} = W_{CNT}/\left[W_{CNT} + (\rho_{CNT}/\rho_m) - (\rho_{CNT}/\rho_m)\, W_{CNT}\right],$$

and W_{CNT} denotes the mass fraction of CNTs in the CNTRC cylinder, and ρ_{CNT} and ρ_m are the mass densities of the CNTs and polymer, respectively.

Similarly, the Poisson's ratio ν_{12} of the FG CNTRC layer is determined as follows:

$$\nu_{12} = V^*_{CNT}\,(\nu_{12})_{CNT} + (V_m\,\nu_m)\,, \tag{3}$$

in which $(\nu_{12})_{CNT}$ and ν_m are the Poisson's ratios of the CNT reinforcements and the polymer matrix, respectively, and ν_{12} is considered as a constant through the thickness coordinate of the FG CNTRC layer.

Using Eqs. (1a-c), (2a-c) and (3), we can obtain the through-thickness distributions of effective properties of FG CNTRC cylinders, which will be applied to the illustrative examples later in this article.

3 Pre-buckling state in a multilayered FGM cylinder

Without loss of generality, we will begin the derivation of a unified formulation for the stability analysis of simply supported, multilayered FGM cylinders under an axial compressive load (P_x). The FG CNTRC cylinders and laminated FRC ones considered in this article can be included as the special cases of multilayered FGM cylinders, such that the former are single-layered FGM ones and the latter are multilayered homogeneous ones.

According to the assumptions of the linear instability approach, a set of membrane stresses exists in the cylinder just before instability occurs. In a symmetrically FG orthotropic cylinder subjected to axial compression, the displacement components of the m^{th}-layer at the initial position are expected in the following form,

$$\bar{u}_x^{(m)} = A_0\,x, \quad \bar{u}_\theta^{(m)} = 0, \quad \text{and} \quad \bar{u}_r^{(m)} = A_0\,\bar{W}_0^{(m)}\,(\zeta) \quad m = 1, 2, \cdots, N_l, \tag{4a-c}$$

where A_0 denotes the assumed uniform axial strain, which is an arbitrary constant, and can be determined later in this article by means of satisfying the force equilibrium equation in the axial direction at edges. In addition, the pre-buckling deformations in the cylinder are assumed to be axisymmetric and plane strain ones.

According to the initial displacement model given in Eq. (4), it is assumed that in the pre-buckling state the cylinder is free of initial shear stresses (i.e., $\bar{\tau}_{xr}^{(m)} = \bar{\tau}_{\theta r}^{(m)} = \bar{\tau}_{x\theta}^{(m)} = 0$, $m = 1, 2, \cdots, N_l$), and the initial normal stresses in the m^{th}-layer can be expressed as

$$\bar{\sigma}_x^{(m)}\,(\zeta) = A_0\,\bar{\sigma}_{x0}^{(m)}\,(\zeta)\,, \quad \bar{\sigma}_\theta^{(m)}\,(\zeta) = A_0\,\bar{\sigma}_{\theta 0}^{(m)}\,(\zeta)\,, \quad \text{and} \quad \bar{\sigma}_r^{(m)}\,(\zeta) = A_0\,\bar{\sigma}_{r0}^{(m)}\,(\zeta)$$
$$m = 1, 2, \cdots, N_l, \tag{5a-c}$$

where

$$\bar{\sigma}_{x0}^{(m)} = Q_{11}^{(m)} + \left(Q_{12}^{(m)}/r\right)\,\bar{W}_0^{(m)} + Q_{13}^{(m)}\,\bar{\sigma}_{r0}^{(m)}\,,$$

$$\bar{\sigma}_{\theta 0}^{(m)} = Q_{12}^{(m)} + \left(Q_{22}^{(m)}/r\right)\bar{W}_0^{(m)} + Q_{23}^{(m)}\,\bar{\sigma}_{r0}^{(m)},$$

$$\bar{\sigma}_{r0}^{(m)} = c_{13}^{(m)} + \left(c_{23}^{(m)}/r\right)\bar{W}_0^{(m)} + c_{33}^{(m)}\left(\bar{W}_0^{(m)},_{\zeta}\right),$$

$$Q_{ij}^{(m)} = c_{ij}^{(m)} - \left(c_{i3}^{(m)}\,c_{j3}^{(m)}/c_{33}^{(m)}\right)\ (i,\ j = 1,\ 2 \text{ and } 6),\ Q_{k3}^{(m)} = c_{k3}^{(m)}/c_{33}^{(m)}\ (k = 1 \text{ and } 2),$$

and $c_{ij}^{(m)}$ denotes the material elastic coefficients of the m^{th}-layer, which is a constant for the multilayered composite cylinder and a function of the thickness coordinate for the FG CNTRC one, while the comma denotes partial differentiation with respect to the suffix variable.

According to the initial displacement model given in Eq. (4), the stress equilibrium equations in the axial and circumferential directions are automatically satisfied, and the one in the radial (or thickness) direction is given as follows:

$$\bar{\sigma}_{r0}^{(m)},_{\zeta} = \left[\left(Q_{23}^{(m)} - 1\right)/r\right]\bar{\sigma}_{r0}^{(m)} + \left(Q_{22}^{(m)}/r^2\right)\bar{W}_0^{(m)} + \left(Q_{12}^{(m)}/r\right). \tag{6}$$

Using Eqs. (5c) and (6), we can write the state space equations of the pre-buckling state of the cylinder in the following form

$$\frac{d\,\bar{\mathbf{F}}^{(m)}}{d\,\zeta} = \bar{\mathbf{K}}^{(m)}\,\bar{\mathbf{F}}^{(m)} + \bar{\mathbf{K}}_p^{(m)}, \tag{7}$$

where

$$\bar{\mathbf{F}}^{(m)} = \begin{Bmatrix} \bar{W}_0^{(m)}(\zeta) \\ \bar{\sigma}_{r0}^{(m)}(\zeta) \end{Bmatrix},\ \bar{\mathbf{K}}^{(m)} = \begin{bmatrix} \bar{k}_{11}^{(m)} & \bar{k}_{12}^{(m)} \\ \bar{k}_{21}^{(m)} & \bar{k}_{22}^{(m)} \end{bmatrix},\ \bar{\mathbf{K}}_p^{(m)} = \begin{Bmatrix} -Q_{13}^{(m)} \\ \left(Q_{12}^{(m)}/r\right) \end{Bmatrix},$$

$$\bar{k}_{11}^{(m)} = -Q_{23}^{(m)}/r,\ \bar{k}_{12}^{(m)} = \left(1/c_{33}^{(m)}\right),\ \bar{k}_{21}^{(m)} = \left(Q_{22}^{(m)}/r^2\right) \text{ and } \bar{k}_{22}^{(m)} = \left(Q_{23}^{(m)} - 1\right)/r.$$

In the cases of pure axial compression, the traction conditions on the lateral surfaces are

$$\bar{\sigma}_r^{(N_l)}(\zeta = h/2) = 0 \quad \text{and} \quad \bar{\sigma}_r^{(1)}(\zeta = -h/2) = 0. \tag{8}$$

By means of Eq. (8), we can readily solve Eq. (7) for the functions of $\bar{W}_0^{(m)}(\zeta)$ and $\bar{\sigma}_{r0}^{(m)}(\zeta)$ using the transfer matrix method combined with the SA one, the solution process of which can be found in Wu and Tsai (2011) and Wu and Jiang (2012), and is thus not repeated here, and the initial membrane stresses can then be obtained as follows:

Taking a free body diagram at each edge, we can express the force equilibrium equation in the axial direction in the following form,

$$\int_0^{2\pi} \int_{\zeta_0}^{\zeta_{N_l}} \bar{\sigma}_x(\zeta)\, r\, d\zeta\, d\theta = -P_x. \tag{9}$$

By satisfying Eq. (9), we subsequently obtain the expression of A_0 as follows:

$$A_0 = -S_x P_x, \tag{10}$$

in which

$$S_x = \left\{ 2\pi R \sum_{m=1}^{N_l} \int_{\zeta_{m-1}}^{\zeta_m} \left[Q_{11}^{(m)} + \left(Q_{12}^{(m)}/r \right) \bar{W}_0^{(m)} + Q_{13}^{(m)}\, \bar{\sigma}_{r0}^{(m)} \right] [1 + (\zeta/R)]\, d\zeta \right\}^{-1}.$$

As a result, the initial in-surface and transverse normal stresses can be obtained as follows:

$$\begin{aligned} &\bar{\sigma}_x^{(m)}(\zeta) = -f_x^{(m)}(\zeta)\, P_x,\ \ \bar{\sigma}_\theta^{(m)}(\zeta) = -f_\theta^{(m)}(\zeta)\, P_x, \\ &\text{and}\ \ \bar{\sigma}_r^{(m)}(\zeta) = -f_r^{(m)}(\zeta)\, P_x, \end{aligned} \tag{11}$$

in which $f_x^{(m)}$, $f_\theta^{(m)}$ and $f_r^{(m)}$ denote the influence functions of the initial in-surface and transverse stresses for the m^{th}-layer of the cylinder in the cases of pure axial compression, and $f_x^{(m)} = S_x \left[Q_{11}^{(m)} + \left(Q_{12}^{(m)}/r \right) \bar{W}_0^{(m)} + Q_{13}^{(m)}\, \bar{\sigma}_{r0}^{(m)} \right]$, $f_\theta^{(m)} = S_x \left[Q_{12}^{(m)} + \left(Q_{22}^{(m)}/r \right) \bar{W}_0^{(m)} + Q_{23}^{(m)}\, \bar{\sigma}_{r0}^{(m)} \right]$, and $f_r^{(m)} = S_x\, \bar{\sigma}_{r0}^{(m)}$. It is well known that the influence of transverse normal stress on the critical load parameters of multilayered FGM cylinders under axial compression is relatively minor, less than 0.1% in most general cases, and this effect is thus neglected in this analysis for brevity.

4 Perturbed state in a multilayered FGM cylinder

4.1 Reissner's mixed variational theorem

As mentioned above, a set of membrane stresses exists in the cylinder just before instability occurs, and this is introduced in the Reissner energy functional of a multilayered FGM cylinder, in which the incremental stresses associated with the small incremental displacements perturbed from the state of neutral equilibrium will be considered.

The incremental stress-strain relations valid for the nature of the symmetry class of elastic materials are given by

$$\begin{Bmatrix} \sigma_x^{(m)} \\ \sigma_\theta^{(m)} \\ \sigma_r^{(m)} \\ \tau_{\theta r}^{(m)} \\ \tau_{xr}^{(m)} \\ \tau_{x\theta}^{(m)} \end{Bmatrix} = \begin{bmatrix} c_{11}^{(m)} & c_{12}^{(m)} & c_{13}^{(m)} & 0 & 0 & 0 \\ c_{12}^{(m)} & c_{22}^{(m)} & c_{23}^{(m)} & 0 & 0 & 0 \\ c_{13}^{(m)} & c_{23}^{(m)} & c_{33}^{(m)} & 0 & 0 & 0 \\ 0 & 0 & 0 & c_{44}^{(m)} & 0 & 0 \\ 0 & 0 & 0 & 0 & c_{55}^{(m)} & 0 \\ 0 & 0 & 0 & 0 & 0 & c_{66}^{(m)} \end{bmatrix} \begin{Bmatrix} \varepsilon_x^{(m)} \\ \varepsilon_\theta^{(m)} \\ \varepsilon_r^{(m)} \\ \gamma_{\theta r}^{(m)} \\ \gamma_{xr}^{(m)} \\ \gamma_{x\theta}^{(m)} \end{Bmatrix}, \tag{12}$$

where $\sigma_x^{(m)}$, $\sigma_\theta^{(m)}$, $\cdots$, $\tau_{x\theta}^{(m)}$ and $\varepsilon_x^{(m)}$, $\varepsilon_\theta^{(m)}$, $\cdots$, $\gamma_{x\theta}^{(m)}$ are the incremental stress and strain components of a certain material point in the m^{th}-layer, respectively. $c_{ij}^{(m)}$ (i, j=1–6) are the elastic coefficients which are constants through the thickness coordinate in the homogeneous elastic layers, and are variable through the thickness coordinate in the FGM layers (i.e., $c_{ij}^{(m)}(\zeta)$ or $c_{ij}^{(m)}(z_m)$).

The kinematic relations between the incremental strainsand the incremental displacements are given by

$$\begin{Bmatrix} \varepsilon_x^{(m)} \\ \varepsilon_\theta^{(m)} \\ \varepsilon_r^{(m)} \\ \gamma_{\theta r}^{(m)} \\ \gamma_{xr}^{(m)} \\ \gamma_{x\theta}^{(m)} \end{Bmatrix} = \begin{bmatrix} \partial_x & 0 & 0 \\ 0 & (1/r)\,\partial_\theta & (1/r) \\ 0 & 0 & \partial_r \\ 0 & (-1/r)+\partial_r & (1/r)\,\partial_\theta \\ \partial_r & 0 & \partial_x \\ (1/r)\,\partial_\theta & \partial_x & 0 \end{bmatrix} \begin{Bmatrix} u_x^{(m)} \\ u_\theta^{(m)} \\ u_r^{(m)} \end{Bmatrix}, \tag{13}$$

where $u_x^{(m)}$, $u_\theta^{(m)}$ and $u_r^{(m)}$ denote the incremental elastic displacement components, $\partial_k = \partial/\partial k \quad (k = x,\ \theta \text{ and } r)$.

The Reissner energy functional of the FGM cylinder under axial compression while in equilibrium in a displaced buckling mode is written in the form of

$$\begin{aligned}\Pi_R = &\sum_{m=1}^{N_l}\int_{-h_m/2}^{h_m/2}\int_{\Omega}\Big[\sigma_x^{(m)}\varepsilon_x^{(m)}+\sigma_\theta^{(m)}\varepsilon_\theta^{(m)}+\sigma_r^{(m)}\varepsilon_r^{(m)}+\tau_{xr}^{(m)}\gamma_{xr}^{(m)}\\ &+\tau_{\theta r}^{(m)}\gamma_{\theta r}^{(m)}+\tau_{x\theta}^{(m)}\gamma_{x\theta}^{(m)}-B(\sigma_{ij}^{(m)})\Big]\,r\,dx\,d\theta\,dz_m\\ &-\sum_{m=1}^{N_l}\int_{-h_m/2}^{h_m/2}\int_{\Omega}(P_x)\left(f_x^{(m)}\hat{\varepsilon}_x^{(m)}+f_\theta^{(m)}\hat{\varepsilon}_\theta^{(m)}\right)r\,dx\,d\theta\,dz_m\\ &-\sum_{m=1}^{N_l}\int_{-h_m/2}^{h_m/2}\int_{\Gamma_\sigma}\bar{T}_i^{(m)}u_i^{(m)}\,d\Gamma\,dz_m\\ &-\sum_{m=1}^{N_l}\int_{-h_m/2}^{h_m/2}\int_{\Gamma_u}T_i^{(m)}(u_i^{(m)}-\bar{u}_i^{(m)})\,d\Gamma\,dz_m\end{aligned} \tag{14}$$

where Ω denotes the cylinder domain on the $x-\theta$ surface; Γ_σ and Γ_u denote the portions of the edge boundary, where the surface tractions $\bar{T}_i^{(m)}$ ($i=x,\ \theta$ and r) and surface displacements $\bar{u}_i^{(m)}$ ($i=x,\ \theta$ and r) perturbed from the state of neutral equilibrium are prescribed, respectively; $B(\sigma_{ij}^{(m)})$ is the complementary energy density function; $\hat{\varepsilon}_x^{(m)}$ and $\hat{\varepsilon}_\theta^{(m)}$ denote the second-order term of the Green-Lagrange in-surface normal strains, and are given by

$$\hat{\varepsilon}_x^{(m)}=\left[\left(u_x^{(m)},_x\right)^2+\left(u_\theta^{(m)},_x\right)^2+\left(u_r^{(m)},_x\right)^2\right]/2, \tag{15}$$

$$\hat{\varepsilon}_\theta^{(m)}=\left[\left(u_\theta^{(m)},_\theta+u_r^{(m)}\right)^2+\left(u_r^{(m)},_\theta-u_\theta^{(m)}\right)^2+\left(u_x^{(m)},_\theta\right)^2\right]/\left(2r^2\right). \tag{16}$$

In this formulation, we take the incremental elastic displacement and incremental transverse stress components as the primary variables subject to variation, and the incremental in- and out-of-surface strain components and the incremental in-surface stress ones are the dependent variables, which can be expressed in terms of the primary variables using Eqs. (12)and (13) as follows:

$$\varepsilon_x^{(m)}=\partial B/\partial\sigma_x^{(m)}=u_x^{(m)},_x, \tag{17}$$

$$\varepsilon_\theta^{(m)}=\partial B/\partial\sigma_\theta^{(m)}=(1/r)\,u_\theta^{(m)},_\theta+(1/r)\,u_r^{(m)}, \tag{18}$$

$$\begin{aligned}\varepsilon_r^{(m)}=\partial B/\partial\sigma_r^{(m)}=&-Q_{13}^{(m)}u_x^{(m)},_x-\left(Q_{23}^{(m)}/r\right)u_\theta^{(m)},_\theta-\left(Q_{23}^{(m)}/r\right)u_r^{(m)}\\ &+\left(1/c_{33}^{(m)}\right)\sigma_r^{(m)},\end{aligned} \tag{19}$$

$$\gamma_{xr}^{(m)} = \partial B/\partial \tau_{xr}^{(m)} = \left(1/c_{55}^{(m)}\right) \tau_{xr}^{(m)}, \tag{20}$$

$$\gamma_{\theta r}^{(m)} = \partial B/\partial \tau_{\theta r}^{(m)} = \left(1/c_{44}^{(m)}\right) \tau_{\theta r}^{(m)}, \tag{21}$$

$$\gamma_{x\theta}^{(m)} = \partial B/\partial \tau_{x\theta}^{(m)} = (1/r)\, u_x^{(m)},_{\theta} + u_{\theta}^{(m)},_{x}. \tag{22}$$

$$\boldsymbol{\sigma}_p^{(m)} = \mathbf{Q}_p^{(m)} \mathbf{B}_1 \mathbf{u}^{(m)} + \mathbf{Q}_p^{(m)} \mathbf{B}_2 u_r^{(m)} + \mathbf{Q}_r^{(m)} \sigma_r^{(m)} \tag{23}$$

where $\boldsymbol{\sigma}_p^{(m)} = \left\{ \begin{array}{ccc} \sigma_x^{(m)} & \sigma_\theta^{(m)} & \tau_{x\theta}^{(m)} \end{array} \right\}^T$, $\mathbf{u}^{(m)} = \left\{ \begin{array}{cc} u_x^{(m)} & u_\theta^{(m)} \end{array} \right\}^T$, $\mathbf{Q}_p^{(m)} = \left[\begin{array}{ccc} Q_{11}^{(m)} & Q_{12}^{(m)} & 0 \\ Q_{12}^{(m)} & Q_{22}^{(m)} & 0 \\ 0 & 0 & Q_{66}^{(m)} \end{array} \right]$, $\mathbf{B}_1 = \left[\begin{array}{cc} \partial_x & 0 \\ 0 & r^{-1}\partial_\theta \\ r^{-1}\partial_\theta & \partial_x \end{array} \right]$,

$$\mathbf{B}_2 = \left[\begin{array}{c} 0 \\ r^{-1} \\ 0 \end{array} \right], \mathbf{Q}_r^{(m)} = \left[\begin{array}{c} Q_{13}^{(m)} \\ Q_{23}^{(m)} \\ 0 \end{array} \right].$$

4.2 Euler-Lagrange equations

Substituting Eqs. (17)–(23) into Eq. (14) and imposing the stationary principle of the Reissner energy functional perturbed from the state of neutral equilibrium (i.e., $\delta \Pi_R = 0$) yields

$$\begin{aligned}
\delta\Pi_R = & \sum_{m=1}^{N_l} \int_{-h_m/2}^{h_m/2} \int_\Omega \left\{ r\sigma_x^{(m)} \delta u_x^{(m)},_{x} + \sigma_\theta^{(m)} \left(\delta u_\theta^{(m)},_{\theta} + \delta u_r^{(m)} \right) \right. \\
& + \tau_{x\theta}^{(m)} (\delta u_x^{(m)},_{\theta} + r\delta u_\theta^{(m)},_{x}) + r\sigma_r^{(m)} \delta u_r^{(m)},_{r} \\
& + \tau_{\theta r}^{(m)} (\delta u_r^{(m)},_{\theta} + r\delta u_\theta^{(m)},_{r} - \delta u_\theta^{(m)}) + r\tau_{xr}^{(m)} (\delta u_r^{(m)},_{x} + \delta u_x^{(m)},_{r}) \\
& + \left[ru_r^{(m)},_{r} + rQ_{13}^{(m)} u_x^{(m)},_{x} + Q_{23}^{(m)} \left(u_\theta^{(m)},_{\theta} + u_r^{(m)} \right) - \left(r\sigma_r^{(m)}/c_{33}^{(m)} \right) \right] \delta\sigma_r^{(m)} \\
& + \left[\left(r^2 u_\theta^{(m)},_{r} - ru_\theta^{(m)} + ru_r^{(m)},_{\theta} - r\tau_{\theta r}^{(m)}/c_{44}^{(m)} \right) \right] \delta\tau_{\theta r}^{(m)} \\
& \left. + \left(ru_x^{(m)},_{r} + ru_r^{(m)},_{x} - r\tau_{xr}^{(m)}/c_{55}^{(m)} \right) \delta\tau_{xr}^{(m)} \right\} dx d\theta dz_m \\
& - \sum_{m=1}^{N_l} \int_{-h_m/2}^{h_m/2} \int_\Omega (P_x) \left\{ \left(rf_x^{(m)} \right) \left[\left(u_x^{(m)},_{x} \right) \left(\delta u_x^{(m)},_{x} \right) + \left(u_\theta^{(m)},_{x} \right) \left(\delta u_\theta^{(m)},_{x} \right) \right. \right. \\
& \left. + \left(u_r^{(m)},_{x} \right) \left(\delta u_r^{(m)},_{x} \right) \right] + \left(f_\theta^{(m)}/r \right) \left[\left(u_\theta^{(m)},_{\theta} + u_r^{(m)} \right) \left(\delta u_\theta^{(m)},_{\theta} + \delta u_r^{(m)} \right) \right. \\
& \left. \left. + \left(u_r^{(m)},_{\theta} - u_\theta^{(m)} \right) \left(\delta u_r^{(m)},_{\theta} - \delta u_\theta^{(m)} \right) + \left(u_x^{(m)},_{\theta} \right) \left(\delta u_x^{(m)},_{\theta} \right) \right] \right\} dx d\theta dz_m \\
& - \sum_{m=1}^{N_l} \int_{-h_m/2}^{h_m/2} \int_{\Gamma_\sigma} \bar{T}_i^{(m)} \delta u_i^{(m)} d\Gamma dz_m - \sum_{m=1}^{N_l} \int_{-h_m/2}^{h_m/2} \int_{\Gamma_u} \delta T_i^{(m)} (u_i^{(m)} - \bar{u}_i^{(m)}) d\Gamma dz_m \\
& = 0
\end{aligned}$$

(24)

where the derivatives of the suffix variables with respect to r are identical to those with respect to z_m (i.e., $dr = dz_m$).

Performing the integration by parts and using Green's theorem, we obtain the Euler–Lagrange equations of 3D elasticity related to the buckling problem of an axially compressed FGM cylinder from the domain integral terms and the admissible boundary conditions from the boundary integral terms, which are written as follows:

The Euler–Lagrange equations are

$$\begin{aligned}\delta u_x^{(m)}: \quad \tau_{xr}^{(m)},_{z_m} = &-\sigma_x^{(m)},_x - \left(\tau_{x\theta}^{(m)},_\theta / r\right) - \left(\tau_{xr}^{(m)}/r\right) - P_x\left(f_x^{(m)}\right)\left(u_x^{(m)},_{xx}\right) \\ &- P_x\left(f_\theta^{(m)}\right)\left(u_x^{(m)},_{\theta\theta}/r^2\right),\end{aligned} \tag{25}$$

$$\begin{aligned}\delta u_\theta^{(m)}: \quad \tau_{\theta r}^{(m)},_{z_m} = &-\tau_{x\theta}^{(m)},_x - \left(\sigma_\theta^{(m)},_\theta / r\right) - 2\left(\tau_{\theta r}^{(m)}/r\right) - P_x\left(f_x^{(m)}\right)\left(u_\theta^{(m)},_{xx}\right) \\ &- P_x\left(f_\theta^{(m)}\right)\left(u_\theta^{(m)},_{\theta\theta} - u_\theta^{(m)} + 2u_r^{(m)},_\theta\right)/r^2,\end{aligned} \tag{26}$$

$$\begin{aligned}\delta u_r^{(m)}: \quad \sigma_r^{(m)},_{z_m} = &-\tau_{xr}^{(m)},_x - \left(\tau_{\theta r}^{(m)},_\theta / r\right) - \left(\sigma_r^{(m)}/r\right) + \left(\sigma_\theta^{(m)}/r\right) \\ &- P_x\left(f_x^{(m)}\right)\left(u_r^{(m)},_{xx}\right) - P_x\left(f_\theta^{(m)}\right)\left(-2u_\theta^{(m)},_\theta + u_r^{(m)},_{\theta\theta} - u_r^{(m)}\right)/r^2,\end{aligned} \tag{27}$$

$$\delta\tau_{xr}^{(m)}: \quad u_x^{(m)},_{z_m} = -u_r^{(m)},_x + \left(\tau_{xr}^{(m)}/c_{55}^{(m)}\right), \tag{28}$$

$$\delta\tau_{\theta r}^{(m)}: \quad u_\theta^{(m)},_{z_m} = \left(u_\theta^{(m)}/r\right) - \left(u_r^{(m)},_\theta / r\right) + \left(\tau_{\theta r}^{(m)}/c_{44}^{(m)}\right), \tag{29}$$

$$\begin{aligned}\delta\sigma_r^{(m)}: \quad u_r^{(m)},_{z_m} = &-\left(c_{13}^{(m)}/c_{33}^{(m)}\right)u_x^{(m)},_x - \left(c_{23}^{(m)}/c_{33}^{(m)}\right)\left(u_\theta^{(m)},_\theta / r\right) \\ &- \left(c_{23}^{(m)}/c_{33}^{(m)}\right)\left(u_r^{(m)}/r\right) + \left(\sigma_r^{(m)}/c_{33}^{(m)}\right),\end{aligned} \tag{30}$$

where $m = 1, 2, \cdots, N_l$.

The lateral boundary conditions are

$$\left[\tau_{xr}^{(N_l)} \quad \tau_{\theta r}^{(N_l)} \quad \sigma_r^{(N_l)}\right] = \left[0 \quad 0 \quad 0\right] \text{ on } z_{N_l} = h_{N_l}/2 \text{ (or } \zeta = h/2), \tag{31a}$$

$$\begin{bmatrix} \tau_{xr}^{(1)} & \tau_{\theta r}^{(1)} & \sigma_r^{(1)} \end{bmatrix} = \begin{bmatrix} 0 & 0 & 0 \end{bmatrix} \text{ on } z_1 = -h_1/2 \text{ (or } \zeta = -h/2); \tag{31b}$$

The edge boundary conditions are

$$\sigma_x^{(m)} n_1 + \tau_{x\theta}^{(m)} n_2 = \bar{T}_x^{(m)} \text{ or } u_x^{(m)} = \bar{u}_x^{(m)}, \tag{32a}$$

$$\tau_{x\theta}^{(m)} n_1 + \sigma_\theta^{(m)} n_2 = \bar{T}_\theta^{(m)} \text{ or } u_\theta^{(m)} = \bar{u}_\theta^{(m)}, \tag{32b}$$

$$\tau_{xr}^{(m)} n_1 + \tau_{\theta r}^{(m)} n_2 = \bar{T}_r^{(m)} \text{ or } u_r^{(m)} = \bar{u}_r^{(m)}, \tag{32c}$$

where $m = 1, 2, \cdots, N_l$, and n_1 and n_2 stand for components of the unit normal vectors on the edges.

The set of Euler–Lagrange Equations (i.e., Eqs. (25)–(30)) associated with a set of appropriate boundary conditions (Eqs. (32a, b, c)) constitutes a well-posed boundary value problem, which is the so-called strong formulation of this problem. A state space DRK method will be developed for the buckling analysis of a simply-supported, multilayered FGM cylinder under axial compression later in this article on the basis of the strong formulation, in which the DRK interpolation functions [Wang et al. (2010)] will be used to construct the shape functions of each primary variable.

5 The state space DRK method

5.1 The single Fourier series expansion method

The single Fourier series expansion method is first applied to reduce this 3D problem to a 2D one. We thus express the primary variables of each individual layer in the following form

$$u_x^{(m)}(x,\theta,\zeta) = \sum_{\hat{n}=0}^{\infty} u_{1\hat{n}}^{(m)}(x,z_m)\cos\hat{n}\theta, \tag{33}$$

$$u_\theta^{(m)}(x,\theta,\zeta) = \sum_{\hat{n}=0}^{\infty} u_{2\hat{n}}^{(m)}(x,z_m)\sin\hat{n}\theta, \tag{34}$$

$$u_r^{(m)}(x,\theta,\zeta) = \sum_{\hat{n}=0}^{\infty} u_{3\hat{n}}^{(m)}(x,z_m)\cos\hat{n}\theta, \tag{35}$$

$$\tau_{xr}^{(m)}(x,\theta,\zeta) = \sum_{\hat{n}=0}^{\infty} \tau_{13\hat{n}}^{(m)}(x,z_m)\cos\hat{n}\theta, \tag{36}$$

$$\tau_{\theta r}^{(m)}(x,\theta,\zeta) = \sum_{\hat{n}=0}^{\infty} \tau_{23\hat{n}}^{(m)}(x,z_m)\sin\hat{n}\theta, \tag{37}$$

$$\sigma_r^{(m)}(x,\theta,\zeta)=\sum_{\hat{n}=0}^{\infty}\sigma_{3\hat{n}}^{(m)}(x,z_m)\cos\hat{n}\theta, \tag{38}$$

where $m=1,2,\cdots,N_l$; $\hat{n}$ denotes the wave number along the θ coordinate, and is a positive integer or zero.

Similarly, the in-surface stresses can be expressed in terms of the primary variables as follows:

$$\sigma_x^{(m)}(x,\theta,\zeta)=\sum_{\hat{n}=0}^{\infty}\sigma_{1\hat{n}}^{(m)}(x,\ z_m)\cos\hat{n}\theta, \tag{39}$$

$$\sigma_\theta^{(m)}(x,\theta,\zeta)=\sum_{\hat{n}=0}^{\infty}\sigma_{2\hat{n}}^{(m)}(x,\ z_m)\cos\hat{n}\theta, \tag{40}$$

$$\tau_{x\theta}^{(m)}(x,\theta,\zeta)=\sum_{\hat{n}=0}^{\infty}\tau_{12\hat{n}}^{(m)}(x,\ z_m)\sin\hat{n}\theta, \tag{41}$$

where $\boldsymbol{\sigma}_{p\hat{n}}^{(m)}=\mathbf{Q}_p^{(m)}\mathbf{B}_{1\hat{n}}\mathbf{u}_{\hat{n}}^{(m)}+\mathbf{Q}_p^{(m)}\mathbf{B}_2u_{3\hat{n}}^{(m)}+\mathbf{Q}_r^{(m)}\sigma_{3\hat{n}}^{(m)}$ in which $\boldsymbol{\sigma}_{p\hat{n}}^{(m)}=\left\{\begin{array}{ccc}\sigma_{1\hat{n}}^{(m)} & \sigma_{2\hat{n}}^{(m)} & \tau_{12\hat{n}}^{(m)}\end{array}\right\}^T$, $\mathbf{u}_{\hat{n}}^{(m)}=\left\{\begin{array}{cc}u_{1\hat{n}}^{(m)} & u_{2\hat{n}}^{(m)}\end{array}\right\}^T$, $\mathbf{B}_{1\hat{n}}=\left[\begin{array}{cc}\partial_x & 0\\ 0 & (\hat{n}/r)\\ -(\hat{n}/r) & \partial_x\end{array}\right]$.

For brevity, the symbols of summation are omitted in the following derivation.

Substituting Eqs. (33)–(38) in the set of Euler-Lagrange equations given in Eqs. (25)–(30), we can obtain a series sets of state space equations governing the buckling of the FGM cylinder for various buckling modes, and they are given as follows:

For the buckling mode $(\hat{n})$,

$$u_{1\hat{n}}^{(m)},_{z_m}=d_{14}^{(m)}\tau_{13\hat{n}}^{(m)}-u_{3\hat{n}}^{(m)},_x, \tag{42}$$

$$u_{2\hat{n}}^{(m)},_{z_m}=d_{22}^{(m)}u_{2\hat{n}}^{(m)}+d_{25}^{(m)}\tau_{23\hat{n}}^{(m)}+d_{26}^{(m)}u_{3\hat{n}}^{(m)}, \tag{43}$$

$$\begin{aligned}\sigma_{3\hat{n}}^{(m)},_{z_m}=&d_{31}^{(m)}u_{1\hat{n}}^{(m)},_x+d_{32}^{(m)}u_{2\hat{n}}^{(m)}+d_{33}^{(m)}\sigma_{3\hat{n}}^{(m)}-\tau_{13\hat{n}}^{(m)},_x-d_{26}^{(m)}\tau_{23\hat{n}}^{(m)}+d_{36}^{(m)}u_{3\hat{n}}^{(m)}\\&-P_x\left(d_1^{(m)}f_\theta^{(m)}u_{2\hat{n}}^{(m)}+f_x^{(m)}u_{3\hat{n}}^{(m)},_{xx}+d_2^{(m)}f_\theta^{(m)}u_{3\hat{n}}^{(m)}\right)\end{aligned}, \tag{44}$$

$$\begin{aligned}\tau_{13\hat{n}}^{(m)},_{z_m}=&\bar{d}_{41}^{(m)}u_{1\hat{n}}^{(m)},_{xx}+d_{41}^{(m)}u_{1\hat{n}}^{(m)}+d_{42}^{(m)}u_{2\hat{n}}^{(m)},_x+d_{43}^{(m)}\sigma_{3\hat{n}}^{(m)},_x+d_{44}^{(m)}\tau_{13\hat{n}}^{(m)}\\&+d_{46}^{(m)}u_{3\hat{n}}^{(m)},_x-P_x\left(f_x^{(m)}u_{1\hat{n}}^{(m)},_{xx}+d_3^{(m)}f_\theta^{(m)}u_{1\hat{n}}^{(m)}\right)\end{aligned}, \tag{45}$$

$$\begin{aligned}\tau_{23\hat{n}}^{(m)},_{z_m}=&-d_{42}^{(m)}u_{1\hat{n}}^{(m)},_x+\bar{d}_{52}^{(m)}u_{2\hat{n}}^{(m)},_{xx}+d_{52}^{(m)}u_{2\hat{n}}^{(m)}+d_{53}^{(m)}\sigma_{3\hat{n}}^{(m)}+d_{55}^{(m)}\tau_{23\hat{n}}^{(m)}\\&+d_{56}^{(m)}u_{3\hat{n}}^{(m)}-P_x\left(f_x^{(m)}u_{2\hat{n}}^{(m)},_{xx}+d_2^{(m)}f_\theta^{(m)}u_{2\hat{n}}^{(m)}+d_1^{(m)}f_\theta^{(m)}u_{3\hat{n}}^{(m)}\right),\end{aligned} \tag{46}$$

$$u^{(m)}_{3\hat{n}},_{z_m} = d^{(m)}_{43} u^{(m)}_{1\hat{n}},_x - d^{(m)}_{53} u^{(m)}_{2\hat{n}} + d^{(m)}_{63} \sigma^{(m)}_{3\hat{n}} + d^{(m)}_{66} u^{(m)}_{3\hat{n}}, \tag{47}$$

where

$$d^{(m)}_{14} = 1/c^{(m)}_{55},\ d^{(m)}_{22} = 1/r,\ d^{(m)}_{25} = 1/c^{(m)}_{44},\ d^{(m)}_{26} = \hat{n}r^{-1},\ d^{(m)}_{31} = Q^{(m)}_{12}/r,$$

$$d^{(m)}_{32} = \hat{n}Q^{(m)}_{22}/r^2,\ d^{(m)}_{33} = \left(Q^{(m)}_{23} - 1\right)/r,\ d^{(m)}_{36} = Q^{(m)}_{22}/r^2,\ \bar{d}^{(m)}_{41} = -Q^{(m)}_{11},$$

$$d^{(m)}_{41} = \hat{n}^2 Q^{(m)}_{66}/r^2,\ d^{(m)}_{42} = -\hat{n}(Q^{(m)}_{12} + Q^{(m)}_{66})/r,\ d^{(m)}_{43} = -Q^{(m)}_{13},\ d^{(m)}_{44} = -1/r,$$

$$d^{(m)}_{46} = -Q^{(m)}_{12}/r,\ \bar{d}^{(m)}_{52} = -Q^{(m)}_{66},\ d^{(m)}_{52} = \hat{n}^2 Q^{(m)}_{22}/r^2,\ d^{(m)}_{53} = \hat{n}Q^{(m)}_{23}/r,$$

$$d^{(m)}_{55} = -2/r,\ d^{(m)}_{56} = \hat{n}Q^{(m)}_{22}/r^2,\ d^{(m)}_{63} = 1/c^{(m)}_{33},\ d^{(m)}_{66} = -Q^{(m)}_{23}/r,$$

$$d^{(m)}_{1} = -2\hat{n}/r^2,\ d^{(m)}_{2} = -\left(\hat{n}^2 + 1\right)/r^2,\ d^{(m)}_{3} = -\hat{n}^2/r^2.$$

The edge boundary conditions of the cylinders are considered as fully simply-supported and are written as follows:

$$u^{(m)}_{2\hat{n}} = u^{(m)}_{3\hat{n}} = \sigma^{(m)}_{1\hat{n}} = 0 \text{ at } x = 0 \text{ and } L, \tag{48}$$

where $m = 1, 2, \cdots, N_l$.

5.2 The DRK interpolation

In this article, the DRK interpolation functions (Wang et al., 2010) are used to construct the shape functions of the primary field variables of this problem, and the DRK interpolation functions and their relevant derivatives are briefly described, as follows.

It is assumed that there are n_p discrete nodes randomly selected and located at $x = x_1,\ x_2, \cdots,\ x_{n_p}$, respectively, in the x direction of the m^{th}-layer, in which a function $F(x,\ z_m)$ is interpolated as $F^a(x,\ z_m)$ and defined as

$$\begin{aligned} F^a(x,\ z_m) &= \sum_{l=1}^{n_p} \psi_l(x) F_l(z_m) \\ &= \sum_{l=1}^{n_p} \left[\bar{\phi}_l(x) + \hat{\phi}_l(x)\right] F_l(z_m) \end{aligned}, \tag{49}$$

where $\bar{\phi}_l(x)$ (l=1, 2,…,n_p) denote the enrichment functions, which are determined by imposing the n^{th}-order reproducing conditions and are given by $\bar{\phi}_l(x) = w_a(x - x_l)\,\mathbf{P}^T(x - x_l)\,\bar{\mathbf{b}}(x)$, in which $\mathbf{P}^T(x - x_l) = \left[\ 1\ \ (x - x_l)\ \ (x - x_l)^2\ \cdots\ (x - x_l)^n\ \right]$, n is the highest order of the basis functions, $\bar{\mathbf{b}}(x)$ is the undetermined function vector,

and $w_a(x-x_l)$ is the weight function centered at the node, $x=x_l$, with a support size a; $\hat{\phi}_l(x)$ (l=1, 2,..., n_p) denote the primitive functions, which are used to introduce the Kronecker delta properties; $\psi_l(x)$ is the shape function of $F^a(x,\, z_m)$ at the sampling node, $x=x_l$; and $F_l(z_m)$ is the nodal function of $F^a(x,\, z_m)$ at $x=x_l$. By selecting the complete n^{th}-order polynomials as the basis functions to be reproduced, we obtain a set of reproducing conditions to determine the undetermined functions of $\bar{b}_i(x)$ $(i=1,2,\cdots,n+1)$ in Eq. (49). These conditions are given as

$$\sum_{l=1}^{n_p}\left[\bar{\phi}_l(x)+\hat{\phi}_l(x)\right]x_l^r=x^r \quad r\le n. \tag{50}$$

Equation (50) represents (n+1) reproducing conditions, and the matrix form of these is given as

$$\begin{aligned}\sum_{l=1}^{n_p}\mathbf{P}(x-x_l)\,\bar{\phi}_l(x) &= \sum_{l=1}^{n_p}\mathbf{P}(x-x_l)\,w_a(x-x_l)\,\mathbf{P}^T(x-x_l)\bar{\mathbf{b}}(x)\\ &= \mathbf{P}(\mathbf{0})-\sum_{l=1}^{n_p}\mathbf{P}(x-x_l)\,\hat{\phi}_l(x)\end{aligned}, \tag{51}$$

where $\mathbf{P}(\mathbf{0})=\left[\begin{array}{ccccc}1 & 0 & 0 & \cdots & 0\end{array}\right]^T$.

According to these conditions, we may obtain the undetermined function vector $\bar{\mathbf{b}}(x)$ in the following form

$$\bar{\mathbf{b}}(x)=\mathbf{A}^{-1}(x)\left[\mathbf{P}(\mathbf{0})-\sum_{l=1}^{n_p}\mathbf{P}(x-x_l)\hat{\phi}_l(x)\right], \tag{52}$$

where $\mathbf{A}(x)=\sum_{l=1}^{n_p}\mathbf{P}(x-x_l)\,w_a(x-x_l)\,\mathbf{P}^T(x-x_l)$.

Substituting Eq. (52) into Eq. (49) yields the shape functions of $F^a(x,z_m)$ in the form of

$$\psi_l(x)=\bar{\phi}_l(x)+\hat{\phi}_l(x) \quad (i=1,\,2,\cdots,\,n_p), \tag{53}$$

where $\bar{\phi}_l(x)=w_a(x-x_l)\mathbf{P}^T(x-x_l)\mathbf{A}^{-1}(x)\left[\mathbf{P}(\mathbf{0})-\sum_{l=1}^{n_p}\mathbf{P}(x-x_l)\,\hat{\phi}(x)\right]$.

It is noted that if we select a set of primitive functions satisfying the Kronecker delta properties (i.e., $\hat{\phi}_l(x_k)=\delta_{lk}$); a priori, then a set of the shape functions with these properties will be obtained (i.e., $\psi_l(x_k)=\delta_{lk}$), due to the fact that the enrichment functions vanish at all the nodes (i.e., $\bar{\phi}_l(x_k)=0$). In this article, a quartic spline function with its support size not covering any neighboring nodes, as suggested by Wang et al. (2010), is assigned to be the primitive function for each sampling

node. Moreover, the derivatives of these DRK interpolation functions are given in Appendix A.

In implementing the present scheme, the weight and primitive functions (i.e., $w(s)$ and $\hat{\phi}(s)$) must be selected in advance. Following Wang et al. (2010), the normalized Gaussian function is selected as the weight function at each sampling node, and this is given as

$$w(s)=\begin{cases}\frac{e^{-(s/\alpha)^2}-e^{-(1/\alpha)^2}}{1-e^{-(1/\alpha)^2}} & \text{for} \quad s\leq 1\\ 0 & \text{for} \quad s>1\end{cases}, \tag{54}$$

where $w_a(x-x_I)=w(s)$, $s=|x-x_I|/a$, and a denotes the radius of the influence zone. The literature [Wang et al. (2010)] suggests an optimal value 0.3 for α for the analysis of elastic solids, and this is also used in this article.

The quartic spline function is selected as the primitive function at each sampling node, and given as

$$\hat{\phi}(s)=\begin{cases}-3s^4+8s^3-6s^2+1 & \text{for} \quad s\leq 1\\ 0 & \text{for} \quad s>1\end{cases}, \tag{55}$$

5.3 The meshless collocation method

Substituting Eqs. (49), (A.1) and (A.6) in the strong formulation of this 3D buckling problem, which consists of the Euler-Lagrange Eqs. (42)–(47) associated with the appropriate boundary conditions in Eqs. (48), we obtain the following sets of ordinary differential equations:

Satisfying the edge conditions given in Eq. (48) yields

$$\left(u_{2\hat{n}}^{(m)}\right)_1=\left(u_{3\hat{n}}^{(m)}\right)_1=0, \text{ and } \left(\sigma_{3\hat{n}}^{(m)}\right)_1=-\left(Q_{11}^{(m)}/Q_{13}^{(m)}\right)\sum_{j=1}^{n_p}\left[\psi_j^{(1)}(x_1)\right]\left(u_{1\hat{n}}^{(m)}\right)_j, \tag{56a}$$

$$\left(u_{2\hat{n}}^{(m)}\right)_{n_p}=\left(u_{3\hat{n}}^{(m)}\right)_{n_p}=0, \text{ and } \left(\sigma_{3\hat{n}}^{(m)}\right)_{n_p}=-\left(Q_{11}^{(m)}/Q_{13}^{(m)}\right)\sum_{j=1}^{n_p}\left[\psi_j^{(1)}(x_{n_p})\right]\left(u_{1\hat{n}}^{(m)}\right)_j. \tag{56b}$$

Using Eqs. (56a) and (56b), we rewrite the Euler-Lagrange equations as follows:

$$\left(u_{1\hat{n}}^{(m)}\right)_{i,z_m}=d_{14}^{(m)}\left(\tau_{13\hat{n}}^{(m)}\right)_i-\sum_{j=2}^{(n_p-1)}\left[\psi_j^{(1)}(x_i)\right]\left(u_{3\hat{n}}^{(m)}\right)_j \quad (i=1,2,\cdots,n_p), \tag{57}$$

$$\left(u_{2\hat{n}}^{(m)}\right)_{i,z_m} = d_{22}^{(m)}\left(u_{2\hat{n}}^{(m)}\right)_i + d_{25}^{(m)}\left(\tau_{23\hat{n}}^{(m)}\right)_i + d_{26}^{(m)}\left(u_{3\hat{n}}^{(m)}\right)_i \quad (i=2,\,3,\cdots,\,(n_p-1)), \tag{58}$$

$$\begin{aligned}\left(\sigma_{3\hat{n}}^{(m)}\right)_{i,z_m} =& d_{31}^{(m)}\sum_{j=1}^{n_p}\left[\psi_j^{(1)}(x_i)\right]\left(u_{1\hat{n}}^{(m)}\right)_j + d_{32}^{(m)}\left(u_{2\hat{n}}^{(m)}\right)_i + d_{33}^{(m)}\left(\sigma_{3\hat{n}}^{(m)}\right)_i \\ & - \sum_{j=1}^{n_p}\left[\psi_j^{(1)}(x_i)\right]\left(\tau_{13\hat{n}}^{(m)}\right)_j - d_{26}^{(m)}\left(\tau_{23\hat{n}}^{(m)}\right)_i \\ & + d_{36}^{(m)}\left(u_{3\hat{n}}^{(m)}\right)_i - P_x d_1^{(m)} f_\theta^{(m)}\left(u_{2\hat{n}}^{(m)}\right)_i \\ & - P_x f_x^{(m)}\sum_{j=2}^{(n_p-1)}\left[\psi_j^{(2)}(x_i)\right]\left(u_{3\hat{n}}^{(m)}\right)_j - P_x d_2^{(m)} f_\theta^{(m)}\left(u_{3\hat{n}}^{(m)}\right)_i \\ & (i=2,\,3,\cdots,\,(n_p-1)),\end{aligned} \tag{59}$$

$$\begin{aligned}\left(\tau_{13\hat{n}}^{(m)}\right)_{i,z_m} =& \bar{d}_{41}^{(m)}\sum_{j=1}^{n_p}\left[\psi_j^{(2)}(x_i)\right]\left(u_{1\hat{n}}^{(m)}\right)_j + d_{41}^{(m)}\left(u_{1\hat{n}}^{(m)}\right)_i \\ & + d_{42}^{(m)}\sum_{j=2}^{(n_p-1)}\left[\psi_j^{(1)}(x_i)\right]\left(u_{2\hat{n}}^{(m)}\right)_j + d_{43}^{(m)}\sum_{j=2}^{(n_p-1)}\left[\psi_j^{(1)}(x_i)\right]\left(\sigma_{3\hat{n}}^{(m)}\right)_j \\ & + \psi_1^{(1)}(x_i)\,Q_{11}^{(m)}\sum_{j=1}^{n_p}\left[\psi_j^{(1)}(x_1)\right]\left(u_{1\hat{n}}^{(m)}\right)_j \\ & + \psi_{n_p}^{(1)}(x_i)\,Q_{11}^{(m)}\sum_{j=1}^{n_p}\left[\psi_j^{(1)}(x_{n_p})\right]\left(u_{1\hat{n}}^{(m)}\right)_j + d_{44}^{(m)}\left(\tau_{13\hat{n}}^{(m)}\right)_i \\ & + d_{46}^{(m)}\sum_{j=2}^{(n_p-1)}\left[\psi_j^{(1)}(x_i)\right]\left(u_{3\hat{n}}^{(m)}\right)_j - P_x f_x^{(m)}\sum_{j=1}^{n_p}\left[\psi_j^{(2)}(x_i)\right]\left(u_{1\hat{n}}^{(m)}\right)_j \\ & - P_x d_3^{(m)} f_\theta^{(m)}\left(u_{1\hat{n}}^{(m)}\right)_i \\ & (i=1,\,2,\,\cdots,\,n_p),\end{aligned} \tag{60}$$

$$\begin{aligned}\left(\tau_{23\hat{n}}^{(m)}\right)_{i,z_m} = & -d_{42}^{(m)}\sum_{j=1}^{n_p}\left[\psi_j^{(1)}(x_i)\right]\left(u_{1\hat{n}}^{(m)}\right)_j + \bar{d}_{52}^{(m)}\sum_{j=2}^{(n_p-1)}\left[\psi_j^{(2)}(x_i)\right]\left(u_{2\hat{n}}^{(m)}\right)_j \\ & + (1-\delta_{i1})(1-\delta_{in_p})\, d_{52}^{(m)}\left(u_{2\hat{n}}^{(m)}\right)_i + (1-\delta_{i1})(1-\delta_{in_p})\, d_{53}^{(m)}\left(\sigma_{3\hat{n}}^{(m)}\right)_i \\ & + d_{55}^{(m)}\left(\tau_{23\hat{n}}^{(m)}\right)_i + (1-\delta_{i1})(1-\delta_{in_p})\, d_{56}^{(m)}\left(u_{3\hat{n}}^{(m)}\right)_i \\ & - \delta_{i1} d_{53}^{(m)}\left(Q_{11}^{(m)}/Q_{13}^{(m)}\right)\sum_{j=1}^{n_p}\left[\psi_j^{(1)}(x_1)\right]\left(u_{1\hat{n}}^{(m)}\right)_j \\ & - \delta_{in_p} d_{53}^{(m)}\left(Q_{11}^{(m)}/Q_{13}^{(m)}\right)\sum_{j=1}^{n_p}\left[\psi_j^{(1)}(x_{n_p})\right]\left(u_{1\hat{n}}^{(m)}\right)_j \\ & - P_x f_x^{(m)}\sum_{j=2}^{(n_p-1)}\left[\psi_j^{(2)}(x_i)\right]\left(u_{2\hat{n}}^{(m)}\right)_j \\ & - (1-\delta_{i1})(1-\delta_{in_p})\, P_x d_2^{(m)} f_\theta^{(m)}\left(u_{2\hat{n}}^{(m)}\right)_i \\ & - (1-\delta_{i1})(1-\delta_{in_p})\, P_x d_1^{(m)} f_\theta^{(m)}\left(u_{3\hat{n}}^{(m)}\right)_i \\ & (i=1,2,\cdots,n_p),\end{aligned} \tag{61}$$

$$\begin{aligned}\left(u_{3\hat{n}}^{(m)}\right)_{i,z_m} = & d_{43}^{(m)}\sum_{j=1}^{n_p}\left[\psi_j^{(1)}(x_i)\right]\left(u_{1\hat{n}}^{(m)}\right)_j - d_{53}^{(m)}\left(u_{2\hat{n}}^{(m)}\right)_i \\ & + d_{63}^{(m)}\left(\sigma_{3\hat{n}}^{(m)}\right)_i + d_{66}^{(m)}\left(u_{3\hat{n}}^{(m)}\right)_i \\ & (i=2,\,3,\cdots,\,(n_p-1)),\end{aligned} \tag{62}$$

where δ_{kl} is the Dirac delta function, in which δ_{kl}=0 when $k \neq l$, and δ_{kl}=1 when $k = l$.

Equations (57)–(62) represent the system of space state equations for the m^{th}-layer for the buckling analysis of simply-supported, multilayered FGM circular hollow cylinders, in which the system consists of $(6n_p - 6)$ simultaneously linear ordinary differential equations in terms of $(6n_p - 6)$ primary variables. These state space equations are rewritten in the matrix form as follows:

$$\frac{d\mathbf{F}^{(m)}}{dz_m} = \mathbf{K}^{(m)}\,\mathbf{F}^{(m)} \quad m = 1,2,\cdots,N_l, \tag{63}$$

in which $\mathbf{F}^{(m)}$ and $\mathbf{K}^{(m)}$ denote the state space variables and the corresponding

coefficient matrix of the m^{th}-layer of the cylinder, respectively, and

$$\mathbf{F}^{(m)} = \left\{ \left(u_{1\hat{n}}^{(m)}\right)_1 \cdots \left(u_{1\hat{n}}^{(m)}\right)_{n_p} \left(u_{2\hat{n}}^{(m)}\right)_2 \cdots \left(u_{2\hat{n}}^{(m)}\right)_{n_p-1} \left(u_{3\hat{n}}^{(m)}\right)_2 \cdots \left(u_{3\hat{n}}^{(m)}\right)_{n_p-1} \right.$$
$$\left. \left(\tau_{13\hat{n}}^{(m)}\right)_1 \cdots \left(\tau_{13\hat{n}}^{(m)}\right)_{n_p} \left(\tau_{23\hat{n}}^{(m)}\right)_1 \cdots \left(\tau_{23\hat{n}}^{(m)}\right)_{n_p} \left(\sigma_{3\hat{n}}^{(m)}\right)_2 \cdots \left(\sigma_{3\hat{n}}^{(m)}\right)_{n_p-1} \right\}^T$$

5.4 Theories of homogeneous linear systems

The general solution of Eq. (63) is

$$\mathbf{F}^{(m)}(z_m) = \mathbf{\Omega}^{(m)}(z_m)\mathbf{L}^{(m)}, \tag{64}$$

where $\mathbf{L}^{(m)}$ is a $(6n_p-6)$ x1 matrix of arbitrary constants; $\mathbf{\Omega}^{(m)}$ is the fundamental matrix of Eq. (63), and is formed by linearly independent solutions in the form of $\mathbf{\Omega}^{(m)} = \left[\mathbf{\Omega}_1^{(m)}, \mathbf{\Omega}_2^{(m)}, \cdots, \quad \mathbf{\Omega}_{(6n_p-6)}^{(m)}\right]$, $\mathbf{\Omega}_i^{(m)} = \mathbf{\Lambda}_i e^{\lambda_i z_m}$ $(i = 1, 2, \cdots, (6n_p-6))$ in which λ_i and Λ_i are the eigenvalues and their corresponding eigenvectors of the coefficient matrix $\mathbf{K}^{(m)}$ in Eq. (63), respectively.

If the coefficient matrix $\mathbf{K}^{(m)}$ has a complex eigenvalue λ_1 (i.e., $\lambda_1 = Re(\lambda_1) + iIm(\lambda_1)$), then its complex conjugate λ_2 (i.e., $\lambda_2 = Re(\lambda_1) - iIm(\lambda_1)$) is also an eigenvalue of $\mathbf{K}^{(m)}$ due to the fact that all of the coefficients of $\mathbf{K}^{(m)}$ are real. In addition, $\mathbf{\Lambda}_{1,2} = Re(\mathbf{\Lambda}_1) \pm iIm(\mathbf{\Lambda}_1)$ are the corresponding eigenvectors of the complex conjugate pair $\lambda_{1,2}$. In order to achieve more efficient computational performance, we replace the complex-valued solutions with another two linearly independent real-valued solutions using Euler's formula, and they are given by

$$\mathbf{\Omega}_1^{(m)} = e^{Re(\boldsymbol{\lambda}_1)z_m}\left[Re(\mathbf{\Lambda}_1)\cos(Im(\lambda_1)z_m) - Im(\mathbf{\Lambda}_1)\sin(Im(\lambda_1)z_m)\right], \tag{65a}$$

$$\mathbf{\Omega}_2^{(m)} = e^{Re(\boldsymbol{\lambda}_1)z_m}\left[Re(\mathbf{\Lambda}_1)\sin(Im(\lambda_1)z_m) + Im(\mathbf{\Lambda}_1)\cos(Im(\lambda_1)z_m)\right]. \tag{65b}$$

On the basis of the previous set of linearly independent real-valued solutions, a transfer matrix method combined with an SA one can be developed for the analysis of FGM circular hollow cylinders, where each FGM layer of the sandwich cylinder is artificially divided into a finite number of individual layers with an equal and small thickness for each layer, compared with the mid-surface radius, as well as with constant material properties, determined in an average thickness sense. The exact solutions of the assorted field variables induced in the FGM cylinder with various edge conditions can thus be gradually approached by increasing the number of individual layers. It is noted that this solution process can be performed layer-by-layer, and the computational performance is independent of the total number of individual layers. Consequently, the implementation of the present approach is much less time-consuming than usual.

5.5 The transfer matrix method

A transfer matrix method for the 3D analysis of simply-supported, multilayered FGM cylinders is developed as follows, in which the FGM cylinder is artificially divided into an N_l-layered cylinder with an equal and small thickness compared with the mid-surface radius of the cylinder. According to Eq. (64), we may obtain the general solution for the state space equations of the m^{th}-layer ($m = 1, 2, \cdots, N_l$).

When $z_m = -h_m/2$, we thus obtain

$$\mathbf{L}^{(m)} = \left[\mathbf{\Omega}^{(m)}(-h_m/2)\right]^{-1} \mathbf{F}_{(m-1)}, \tag{66}$$

where $\mathbf{F}_{(m-1)}$ denotes the vector of state space variables at the interface between the $(m\text{-}1)^{th}$- and m^{th}-layers, and $\mathbf{F}_{(m-1)} = \mathbf{F}^{(m)}(z_m = -h_m/2)$.

Using Eqs. (64) and (66), we obtain

$$\mathbf{F}_{(m)} = \mathbf{R}_{(m)}\, \mathbf{F}_{(m-1)}, \tag{67}$$

where $\mathbf{R}_{(m)} = \mathbf{\Omega}^{(m)}(z_m)\ \left[\mathbf{\Omega}^{(m)}(-h_m/2)\right]^{-1}$.

By analogy, the vectors of state space variables between the top and bottom surfaces of the cylinder (i.e., $\mathbf{F}_{(N_l)}$ and $\mathbf{F}_{(0)}$) are linked by

$$\begin{aligned}\mathbf{F}_{(N_l)} &= \mathbf{R}_{(N_l)}\, \mathbf{F}_{(N_l-1)} \\ &= \left(\prod_{m=1}^{N_l} \mathbf{R}_{(m)}\right) \mathbf{F}_{(0)}.\end{aligned} \tag{68}$$

where $\prod_{m=1}^{N_l} \mathbf{R}_{(m)} = \mathbf{R}_{(N_l)}\mathbf{R}_{(N_l-1)} \cdots \mathbf{R}_{(2)}\, \mathbf{R}_{(1)}$.

Equation (68) represents the sets of $(6n_p - 6)$ simultaneous algebraic equations. Imposing the traction free conditions on the lateral surfaces, we may rewrite it as

$$\begin{bmatrix} \mathbf{u}_u \\ \boldsymbol{\sigma}_u \end{bmatrix} = \begin{bmatrix} \mathbf{R}_{\mathbf{I\ I}} & \mathbf{R}_{\mathbf{I\ II}} \\ \mathbf{R}_{\mathbf{II\ I}} & \mathbf{R}_{\mathbf{II\ II}} \end{bmatrix} \begin{bmatrix} \mathbf{u}_b \\ \boldsymbol{\sigma}_b \end{bmatrix}, \tag{69}$$

where $\mathbf{u}_u$ and $\mathbf{u}_b$ denote the nodal displacement components on the upper and bottom surfaces, respectively, $\boldsymbol{\sigma}_u$ and $\boldsymbol{\sigma}_b$ the nodal transverse stress components on the upper and bottom surfaces, respectively and they are given as follows:

$$\begin{aligned}\mathbf{u}_u = \Big\{ &\left(u_1^{(N_l)}(\zeta = 0.5h)\right)_1, \cdots, \left(u_1^{(N_l)}(\zeta = 0.5h)\right)_{n_p}, \left(u_2^{(N_l)}(\zeta = 0.5h)\right)_2, \cdots, \\ &\left(u_2^{(N_l)}(\zeta = 0.5h)\right)_{n_p-1}, \left(u_3^{(N_l)}(\zeta = 0.5h)\right)_2, \cdots, \left(u_3^{(N_l)}(\zeta = 0.5h)\right)_{n_p-1} \Big\}^T\end{aligned}$$

$$\mathbf{u}_b = \left\{ \left(u_1^{(1)}(\zeta=-0.5h)\right)_1, \cdots, \left(u_1^{(1)}(\zeta=-0.5h)\right)_{n_p}, \left(u_2^{(1)}(\zeta=-0.5h)\right)_2, \cdots, \right.$$
$$\left. \left(u_2^{(1)}(\zeta=-0.5h)\right)_{n_p-1}, \left(u_3^{(1)}(\zeta=-0.5h)\right)_2, \cdots, \left(u_3^{(1)}(\zeta=-0.5h)\right)_{n_p-1} \right\}^T$$

$$\boldsymbol{\sigma}_u = \left\{ \left(\tau_{13}^{(N_l)}(\zeta=0.5h)\right)_1, \cdots, \left(\tau_{13}^{(N_l)}(\zeta=0.5h)\right)_{n_p}, \left(\tau_{23}^{(N_l)}(\zeta=0.5h)\right)_1, \cdots, \right.$$
$$\left. \left(\tau_{23}^{(N_l)}(\zeta=0.5h)\right)_{n_p}, \left(\sigma_3^{(N_l)}(\zeta=0.5h)\right)_2, \cdots, \left(\sigma_3^{(N_l)}(\zeta=0.5h)\right)_{n_p-1} \right\}^T$$

$$\boldsymbol{\sigma}_b = \left\{ \left(\tau_{13}^{(1)}(\zeta=-0.5h)\right)_1, \cdots, \left(\tau_{13}^{(1)}(\zeta=-0.5h)\right)_{n_p}, \left(\tau_{23}^{(1)}(\zeta=-0.5h)\right)_1, \cdots, \right.$$
$$\left. \left(\tau_{23}^{(1)}(\zeta=-0.5h)\right)_{n_p}, \left(\sigma_3^{(1)}(\zeta=-0.5h)\right)_2, \cdots, \left(\sigma_3^{(1)}(\zeta=-0.5h)\right)_{n_p-1} \right\}^T$$

Imposing the traction free conditions on the lateral surfaces, which are $\boldsymbol{\sigma}_u = \mathbf{0}$ and $\boldsymbol{\sigma}_b = \mathbf{0}$, and using the least square method to form a system of algebraic equations with a square coefficient matrix, we obtain

$$\mathbf{A}^T \mathbf{A} \mathbf{u}_u = \mathbf{0}, \tag{70}$$

where $\mathbf{A} = \mathbf{R}_{\mathbf{II}} (\mathbf{R}_{\mathbf{II}})^{-1}$,

A nontrivial solution of Eq. (69) exists if the determinant of the coefficient matrix $(\mathbf{A}^T \mathbf{A})$ vanishes. Hence, the critical load can be obtained by

$$\left| \mathbf{A}^T \mathbf{A} \right| = 0. \tag{71}$$

Because Eq. (71) yields an implicit, rather than explicit, function of $(P_x)_{cr}$, a bi-section method is used to determine the roots of Eq. (71) with a fixed value of $\hat{n}$.

6 Illustrative Examples

6.1 Laminated FRC cylinders

Based on the theory 3D elasticity, Noor and Peters (1989) and Ye and Soldatos (1995) presented the exact 3D solutions for the critical loads of simply-supported, $[0°/90°]_{20}$ laminated circular hollow cylinders under axial compression, and these benchmark solutions are used to validate the accuracy and convergence of the ones obtained using the state space DRK method in Table 1, in which the fibers of the different layers alternate between the circumferential and longitudinal directions, with the fibers of the top and bottom layers running in the circumferential and longitudinal directions, respectively; the geometric parameters of the cylinders are $L/R = 5$ and h/R =0.2; the material properties of the cylinders are given as

$$E_L/E_T = 15,\ G_{LT}/E_T = 0.5,\ G_{TT}/E_T = 0.35 \text{ and } \upsilon_{LL} = \upsilon_{LT} = 0.3, \tag{72a-d}$$

where the subscripts of L and T denote the directions parallel and transverse to the fiber directions, respectively.

Table 1: Convergence studies for the state space DRK solutions of the critical load parameters of simply-supported, laminated $[0^\circ/90^\circ]_{20}$ cylinders under axial compression ($(\bar{P}_x)_{cr} = (P_x)_{cr}R^2/(2\pi RE_T h^3)$).

n	a	Theories	n_p	$\hat{n}=1$	$\hat{n}=2$	$\hat{n}=3$
3	$3.1\Delta x$	Present	19	5.5123	5.0301	6.7959
			21	5.5123	5.0317	6.8572
			25	5.5123	5.0365	7.0068
			29	5.5123	5.0365	7.1230
3	$3.6\Delta x$	Present	19	5.5203	4.9481	6.1100
			21	5.5203	4.9823	6.2325
			25	5.5203	4.9863	6.5174
			29	5.5203	4.9887	6.6925
4	$4.1\Delta x$	Present	19	5.5115	5.0349	6.9201
			21	5.5115	5.0277	6.9774
			25	5.5115	5.0293	6.9169
			29	5.5115	5.0293	7.0187
4	$4.6\Delta x$	Present	19	5.5147	5.0094	6.7967
			21	5.5147	5.0309	6.8644
			25	5.5147	5.0352	6.9917
			29	5.5147	5.0352	6.9232
ED2 (D'Ottavio and Carrera, 2010)				5.512	5.187	NA
ED4 (D'Ottavio and Carrera, 2010)				5.511	5.073	NA
EMZ4 (D'Ottavio and Carrera, 2010)				5.511	5.056	NA
LM4 (D'Ottavio and Carrera, 2010)				5.511	5.052	NA
3D elasticity (Noor and Peters, 1989)				5.511	5.052	NA
3D elasticity (Ye and Soldatos, 1995)				5.520	5.051	NA
Modified Pagano (Wu and Tsai, 2012)				5.512	5.042	7.129

For comparison purposes, the critical load parameter, $(\bar{P}_x)_{cr}$, is defined as

$$(\bar{P}_x)_{cr} = (P_x)_{cr}R^2/\left(2\pi RE_T h^3\right). \tag{73}$$

Table 1 shows the convergence studies for the state space DRK solutions of the critical load parameters of simply-supported, $[0^\circ/90^\circ]_{20}$ laminated cylinders under axial compression for different buckling modes, $\hat{n} = 1-3$, in which the highest order of base functions (n) is taken to be n=3 and 4, the uniform distribution of nodes (n_p) is n_p=19, 21, 25 and 29, and the radius of the influence zone for each

Table 2: The state space DRK solutions of the critical load parameters of simply-supported, laminated $\left[0^0/90^0\right]_s$ and $\left[0^0/90^0/0^0/90^0\right]_s$ cylinders under axial compression (n=3a=3.1Δx , $n_p = 25$, L/R=5, h/R=0.2, and $(\bar{P}_x)_{cr} = (P_x)_{cr} R^2/\left(2\pi R E_T h^3\right)$).

Laminates	$(\hat{m},\ \hat{n})$	Theories	E_L/E_T				
			5	10	20	30	40
$\left[0°/90°\right]_s$	(2, 2)	Present (N_l= 4)	3.4355	4.3831	5.6691	6.6447	7.4564
		Present (N_l= 8)	3.4351	4.3837	5.6707	6.6527	7.4644
		Present (N_l=16)	3.4354	4.3838	5.6715	6.6527	7.4644
		Present (N_l=32)	3.4354	4.3838	5.6715	6.6527	7.4644
		Present (N_l=40)	3.4354	4.3839	5.6715	6.6527	7.4644
		ED2 (D'Ottavio and Carrera, 2010)	3.463	4.445	5.825	6.918	7.860
		ED4 (D'Ottavio and Carrera, 2010)	3.443	4.395	5.705	6.705	7.540
		EMZ4 (D'Ottavio and Carrera, 2010)	3.443	4.398	5.703	6.698	7.528
		LM4 (D'Ottavio and Carrera, 2010)	3.443	4.393	5.688	6.668	7.480
		Modified Pagano (Wu and Tsai, 2012)	3.436	4.386	5.679	6.659	7.471
		ANSYS (4x12x16)	3.6267	4.4806	5.5833	6.5801	7.2322
		ANSYS (8x25x16)	3.6166	4.4691	5.5711	6.5763	7.2437
		ANSYS (16x50x16)	3.6165	4.4692	5.5720	6.5791	7.2448
$\left[0°/90°/0°/90°\right]_s$	(3, 2)	Present (N_l= 8)	3.9368	4.9899	6.3638	7.5681	8.4432
		Present (N_l=16)	3.9368	4.9901	6.3646	7.5678	8.4511
		Present (N_l=32)	3.9368	4.9901	6.3646	7.5678	8.4511
		Present (N_l=40)	3.9368	4.9901	6.3646	7.5678	8.4511
		ED2 (D'Ottavio and Carrera, 2010)	3.980	5.083	6.678	7.903	8.903
		ED4 (D'Ottavio and Carrera, 2010)	3.953	5.018	6.518	7.635	8.525
		EMZ4 (D'Ottavio and Carrera, 2010)	3.953	5.015	6.513	7.623	8.508
		LM4 (D'Ottavio and Carrera, 2010)	3.953	5.013	6.503	7.605	8.483
		Modified Pagano (Wu and Tsai, 2012)	3.946	5.005	6.494	7.598	8.475
		ANSYS (4x12x32)	4.0457	4.9730	6.3094	7.3248	8.2479
		ANSYS (8x25x32)	4.0518	4.9828	6.3272	7.3499	8.2798
		ANSYS (16x50x32)	4.0570	4.9917	6.3439	7.3738	8.3100

sampling node (a) is $a = 3.1\Delta x$ and $3.6\Delta x$ when n=3, and $a = 4.1\Delta x$ and $4.6\Delta x$ when n=4, while $\Delta x = L/(n_p - 1)$. It can be seen from Table 1 that the solutions are slightly affected by changing the radius of the influence zone, and the solutions converge at n_p=19, 25 and 29 for the buckling modes of $\hat{n} = 1$, 2 and 3, respectively. The convergent solutions are obtained when both n=3, $a = 3.1\Delta x$ and n=4, $a = 4.1\Delta x$ are used, and these are in excellent agreement with the 3D elasticity solutions [Noor and Peters (1989); Ye and Soldatos (1995)] and the ones obtained using the modified Pagano method. These convergent solutions of the state space DRK method are also compared with the solutions obtained using the equivalent single-layered theories with second- and fourth-order displacement models (i.e., ED2 and ED4), those using with fourth-order mixed models combined with a zig-zag function (EMZ4), and those using layerwise theories with the fourth-order mixed models (LM4), and these are shown to be closely agree with the solutions obtained using LM4 and EMZ4. In addition, results show that the performance among the above-mentioned 2D and approximate 3D theories available in the literature is LM4>EMZ4>ED4>ED2, in which the symbol ">" means more accurate and a faster convergence rate.

Table 2 shows the state space DRK solutions for the critical load parameters of axially loaded, $[0^\circ/90^\circ]_s$ and $[0^\circ/90^\circ/0^\circ/90^\circ]_s$ laminated cylinders with fully simply supported edges, in which the material properties, geometrical parameters, and critical load parameters are the same as those in Table 1, and n=3, $a = 3.1\Delta x$ and n_p=25 are adopted based on the conclusions of the convergence studies shown in Table 1. It can be seen in Table 2 that the state space DRK solutions converge when the total number of artificially divided layers (N_l) is taken to be N_l=16, and these sixteen-layer solutions are in excellent agreement with the modified Pagano solutions [Wu and Tsai (2012)] and LM4 ones [D'Ottavio and Carrera (2010)]. The state space DRK solutions are also compared with the solutions obtained using the refined and advanced 2D theories by D'Ottavio and Carrera (2010), such as ED2, ED4, EMZ4 and LM4, the modified Pagano solutions, and the ANSYS commercial software using 3D brick element with (4x12x16), (8x25x16) and (16x50x16) meshes in the (x, θ, ζ) axes. Again, the performance of these 2D refined and advanced theories is shown to be LM4>EMZ4>ED4>ED2. The relative errors between the modified Pagano solutions and sixteen-layer state space DRK ones are less than 0.5%, while those between the modified Pagano solutions and ANSYS ones using a mesh (16x50x16) for $[0^\circ/90^\circ]_s$ laminated cylinders and a mesh (16x50x32) for $[0^\circ/90^\circ/0^\circ/90^\circ]_s$ laminated ones are below 3%. In addition, the critical load parameters increase when the value of orthotropic ratio (E_L/E_T) becomes greater, which implies that the gross stiffness of the cylinder becomes greater.

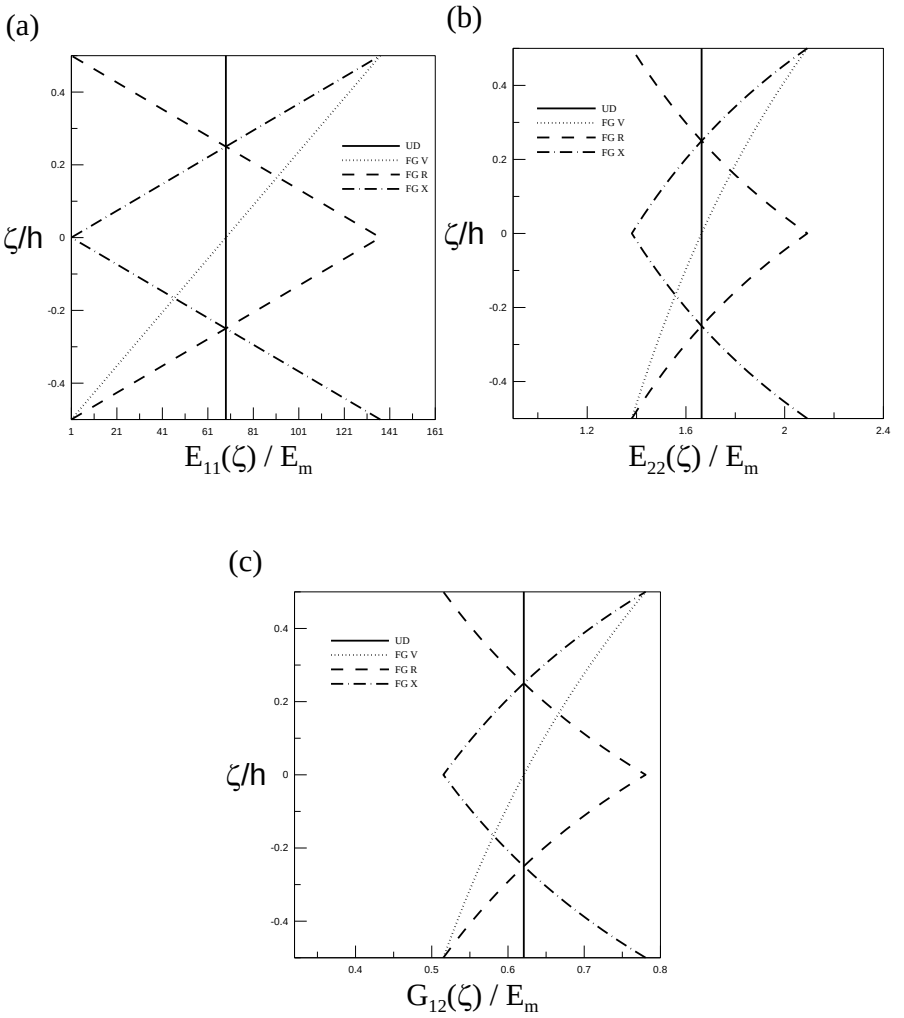

Figure 2: The through-thickness distributions of Young's and shear moduli for an FG CNTRC cylinder with $V^*_{CNT} = 0.17$ (a) E_{11} (b) E_{22} (c) G_{12}

6.2 CNTRC hollow cylinders

In this section, the buckling analysis of simply-supported, single-layered CNTRC circular hollow cylinders under axial compression is carried out, in which PmPV [Han and Elliott (2007)] is used as the matrix, the material properties of which are ν_m=0.34 and E_m=2.1 GPa at room temperature (300K), and armchair (10, 10) single-walled CNTs are used as the reinforcements, the material properties of

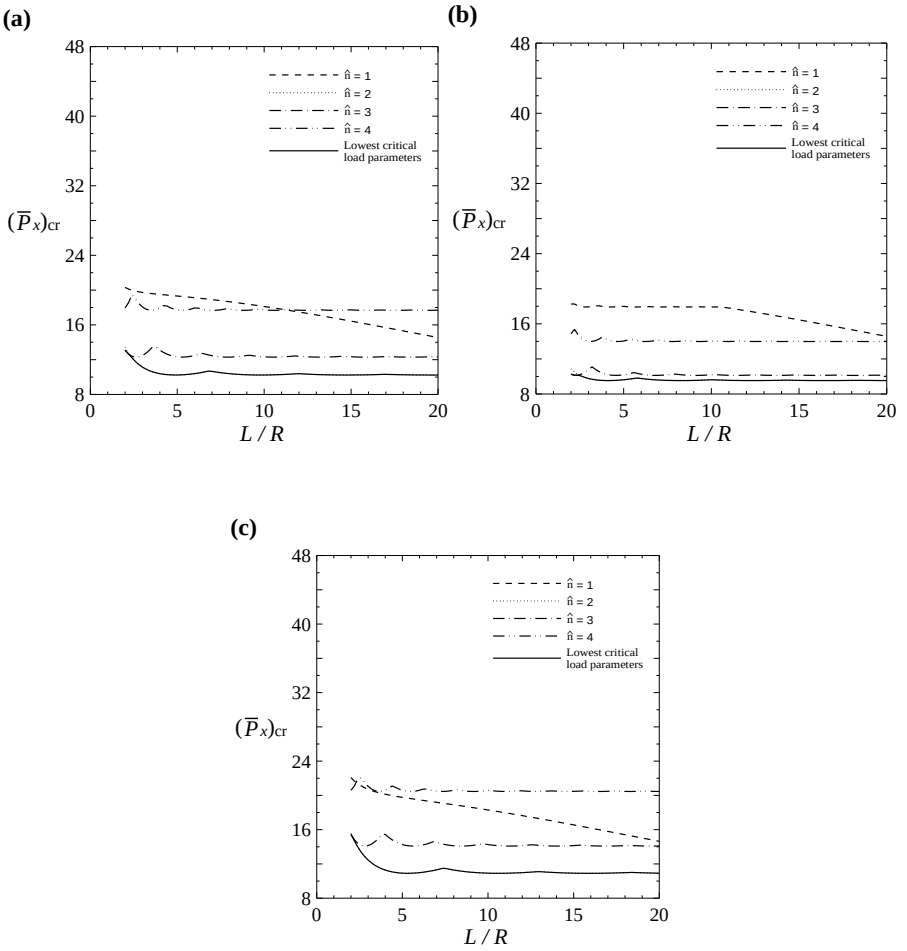

Figure 3: Variations of the critical load parameters of axially loaded and simply-supported, FG CNTRC cylinders with the length-to-radius ratio for $\hat{n} = 1-4$, $R/h = 10$ and $V^*_{CNT} = 0.11$ (a) UD, (b) FG R-type, (c) FG X-type.

which are $(E_{11})_{CNT}$=5646.6GPa, $(E_{22})_{CNT} = (E_{33})_{CNT}$=7080.0 GPa, $(G_{12})_{CNT} = (G_{13})_{CNT} = (G_{23})_{CNT}$=1944.5 GPa and $(\nu_{12})_{CNT} = (\nu_{13})_{CNT} = (\nu_{23})_{CNT}$=0.175 (Zhang and Shen, 2006). In addition, the CNT efficiency parameters η_k (k=1-3) given in Eqs. (1a-c) are taken to be η_1=0.149 and $\eta_2 = \eta_3$=0.934 in the case of V^*_{CNT}=0.11, η_1=0.150 and $\eta_2 = \eta_3$=0.941 in the case of V^*_{CNT}=0.14, and η_1=0.149 and $\eta_2 = \eta_3$=1.381 in the case of V^*_{CNT}=0.17, and these were determined by equalizing the elastic properties of CNTRC plates obtained using the rule of mix-

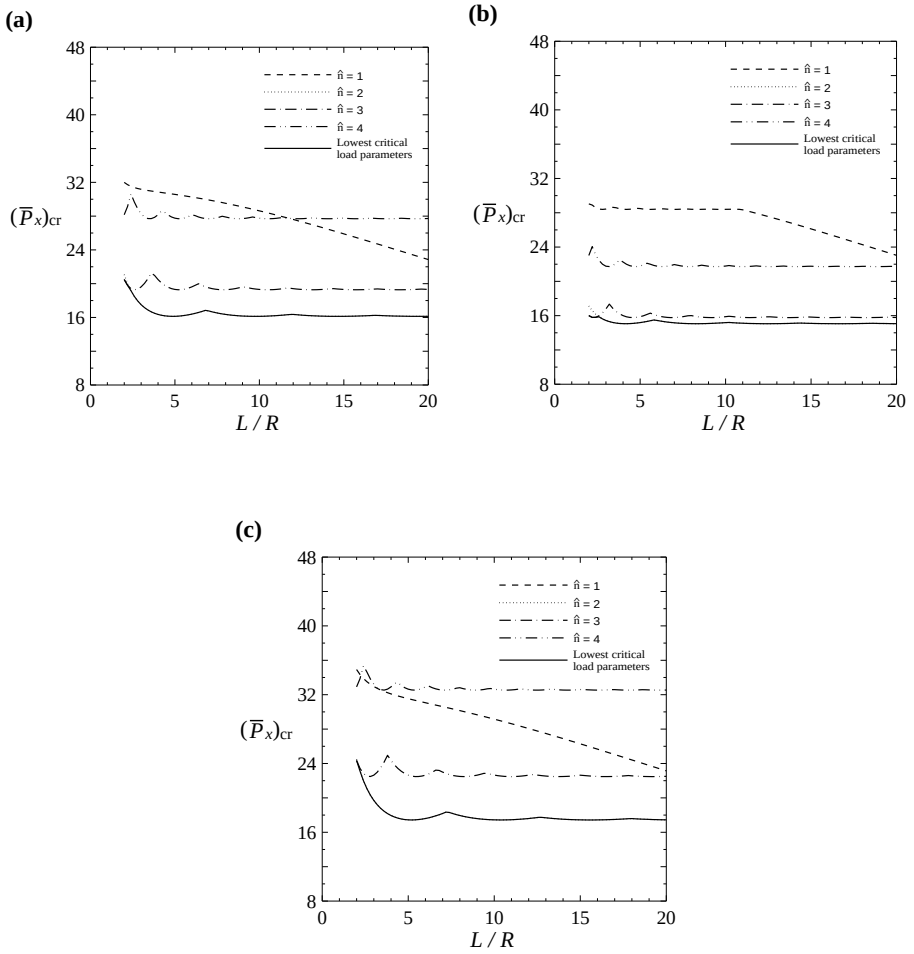

Figure 4: Variations of the critical load parameters of axially loaded and simply-supported, FG CNTRC cylinders with the length-to-radius ratio for $\hat{n} = 1 - 4$, $R/h = 10$ and $V^*_{CNT} = 0.17$ (a) UD, (b) FG R-type, (c) FG X-type.

tures and molecular dynamics simulation (Han and Elliott, 2007). The variations of the Young's moduli, E_{11} and E_{22}, and shear modulus, G_{12}, with the thickness coordinate of the CNTRC cylinder for different CNT distributions, UD and FG R- and X-type distributions, in the case of V^*_{CNT}=0.17, are shown in Fig. 2, and note that the integrations of these moduli through the thickness coordinate are identical to one another. Moreover, the dimensionless critical load parameter is defined as $(\bar{P}_x)_{cr} = (P_x)_{cr} R^2 / \left(2\pi R E_m h^3\right)$.

Table 3: Convergence studies for the state space DRK solutions of the critical load parameters of simply-supported, FG CNTRC cylinders under axial compression (n=3,a=3.1Δx , $n_p = 15$, L/R=5, R/h=10, and $(\bar{P}_x)_{cr} = (P_x)_{cr}R^2/(2\pi RE_m h^3)$).

V^*_{CNT}	$\hat{n}$	Theories	CNT distributions		
			UD-type	FG R-type	FG X-type
0.11	1	Present ($N_l = 5$)	19.2832	18.4827	20.3559
		Present ($N_l = 10$)	19.2840	19.0302	19.6978
		Present ($N_l = 20$)	19.2848	19.0214	19.7113
		Present ($N_l = 40$)	19.2848	19.0198	19.7153
		Modified Pagano (Wu and Tsai, 2012)	19.3162	18.9896	19.7674
	2	Present ($N_l = 5$)	10.2098	9.4045	11.1130
		Present ($N_l = 10$)	10.2114	9.6241	10.8114
		Present ($N_l = 20$)	10.2122	9.6066	10.8305
		Present ($N_l = 40$)	10.2122	9.6034	10.8353
		Modified Pagano (Wu and Tsai, 2012)	10.2307	9.6187	10.9164
	3	Present ($N_l = 5$)	12.0886	9.8883	14.4194
		Present ($N_l = 10$)	12.0894	9.9663	14.1600
		Present ($N_l = 20$)	12.0902	9.9018	14.2269
		Present ($N_l = 40$)	12.0902	9.8891	14.2428
		Modified Pagano (Wu and Tsai, 2012)	12.3189	10.1867	14.2538
0.14	1	Present ($N_l = 5$)	20.3241	19.5323	21.5727
		Present ($N_l = 10$)	20.3257	20.0647	20.9018
		Present ($N_l = 20$)	20.3257	20.0559	20.9209
		Present ($N_l = 40$)	20.3257	20.0543	20.9257
		Modified Pagano (Wu and Tsai, 2012)	20.3695	19.5656	20.9843
	2	Present ($N_l = 5$)	10.9706	10.0705	12.0815
		Present ($N_l = 10$)	10.9721	10.2798	11.7735
		Present ($N_l = 20$)	10.9729	10.2567	11.7997
		Present ($N_l = 40$)	10.9729	10.2528	11.8061
		Modified Pagano (Wu and Tsai, 2012)	11.0159	10.2553	11.9105
	3	Present ($N_l = 5$)	13.5528	10.8480	16.3961
		Present ($N_l = 10$)	13.5544	10.8735	16.1399
		Present ($N_l = 20$)	13.5552	10.7899	16.2227
		Present ($N_l = 40$)	13.5552	10.7716	16.2434
		Modified Pagano (Wu and Tsai, 2012)	13.6900	11.0757	16.0276
0.17	1	Present ($N_l = 5$)	30.5164	29.6394	32.4039
		Present ($N_l = 10$)	30.5180	30.3763	31.4148
		Present ($N_l = 20$)	30.5188	30.3723	31.4450
		Present ($N_l = 40$)	30.5188	30.3715	31.4530
		Modified Pagano (Wu and Tsai, 2012)	30.5658	28.4854	31.5316
	2	Present ($N_l = 5$)	16.0977	14.9025	17.7203
		Present ($N_l = 10$)	16.1001	15.1905	17.2882
		Present ($N_l = 20$)	16.1001	15.1643	17.3272
		Present ($N_l = 40$)	16.1009	15.1603	17.3367
		Modified Pagano (Wu and Tsai, 2012)	16.1271	15.1820	17.4399
	3	Present ($N_l = 5$)	18.9299	15.4587	22.7281
		Present ($N_l = 10$)	18.9323	15.5327	22.3509
		Present ($N_l = 20$)	18.9331	15.4309	22.4599
		Present ($N_l = 40$)	18.9331	15.4118	22.4878
		Modified Pagano (Wu and Tsai, 2012)	19.3126	15.8701	22.6490

Table 4: The state space DRK solutions of the critical load parameters of simply-supported, CNTRC cylinders under axial compression (n=3,a=3.1Δx , $n_p = 15$, L/R=5, $V^*_{CNT} = 0.11$, and $(\bar{P}_x)_{cr} = (P_x)_{cr}R^2/(2\pi RE_m h^3)$).

R/h	$\hat{n}$	Theories	CNT distributions		
			UD-type	FG R-type	FG X-type
5	1	Present ($N_l = 5$)	5.3215	4.9247	5.7671
		Present ($N_l = 10$)	5.3226	5.0441	5.6000
		Present ($N_l = 20$)	5.3226	5.0338	5.6091
		Present ($N_l = 40$)	5.3226	5.0316	5.6113
		Modified Pagano (Wu and Tsai, 2012)	5.3322	5.0453	5.6189
	2	Present ($N_l = 5$)	4.6701	4.0846	5.2783
		Present ($N_l = 10$)	4.6712	4.1619	5.1498
		Present ($N_l = 20$)	4.6723	4.1483	5.1646
		Present ($N_l = 40$)	4.6723	4.1460	5.1691
		Modified Pagano (Wu and Tsai, 2012)	4.6747	4.1606	5.1673
	3	Present ($N_l = 5$)	7.4689	6.3696	7.9532
		Present ($N_l = 10$)	7.1688	5.9797	7.7872
		Present ($N_l = 20$)	7.2631	5.9342	7.7940
		Present ($N_l = 40$)	7.2188	5.9137	7.8111
		Modified Pagano (Wu and Tsai, 2012)	7.2442	5.9498	7.9220
20	1	Present ($N_l = 5$)	58.8646	45.9594	68.4366
		Present ($N_l = 10$)	58.8600	44.6543	67.8455
		Present ($N_l = 20$)	58.8600	43.9268	67.9364
		Present ($N_l = 40$)	58.8555	43.7449	67.9819
		Modified Pagano (Wu and Tsai, 2012)	58.5862	45.6923	66.4633
	2	Present ($N_l = 5$)	31.5491	30.1258	33.3771
		Present ($N_l = 10$)	31.5491	30.9716	32.3767
		Present ($N_l = 20$)	31.5491	30.9579	32.3994
		Present ($N_l = 40$)	31.5491	30.9579	32.4085
		Modified Pagano (Wu and Tsai, 2012)	31.5171	30.9681	32.3614
	3	Present ($N_l = 5$)	23.6732	22.0134	26.7198
		Present ($N_l = 10$)	23.6732	22.0634	26.0650
		Present ($N_l = 20$)	23.6732	21.8906	26.1423
		Present ($N_l = 40$)	23.6732	21.8542	26.1605
		Modified Pagano (Wu and Tsai, 2012)	23.8796	21.3099	26.5538

Tables 3 and 4 show the convergence studies of the state space DRK solutions when varying the number of individual layers (N_l) for the critical load parameters of axially loaded and simply-supported FG CNTRC cylinders with different CNT distributions, volume fractions of CNTs, wave number in the circumferential coordinate, and the radius-to-thickness ratio, in which n=3, $a = 3.1\Delta x$, n_p=15, L/R=5, R/h=5, 10 and 20, and V^*_{CNT}=0.11, 0.14 and 0.17. It can be seen that the convergent solutions are obtained at N_l=20, and these are in excellent agreement with the 3D elasticity solutions obtained using the modified Pagano method (Wu and Tsai, 2012). The critical load of a CNTRC cylinder increases when the volume fraction

of CNTs becomes larger and the radius-to-thickness ratio smaller, which implies that the cylinder becomes stiffer, and these values for the cases of UD and FG R- and X-type CNT distributions are FG X-type > UD >FG R-type, in which ">" means larger, which reflects the fact that CNT reinforcements distributed close to the top and bottom surfaces are more efficient than those distributed near the mid-surface with regard to enhancing the stiffness of the CNTRC cylinders, and this is also found in Lei et al. (2013). Moreover, the lowest critical load parameter occurs at the second wave number in the circumferential coordinate ($\hat{n} = 2$) in the case of R/h=10, and thus will not be affected by changing the values of V^*_{CNT}.

Figures 3 and 4 show variations of the critical load parameters of axially-loaded and simply-supported, FG CNTRC cylinders with the length-to-radius ratio for V^*_{CNT}=0.11 and 0.17, respectively, in which $\hat{n}$=1-4 and R/h=10, and the CNT distributions are UD, R-type and X-type ones. Referring to the figures, the magnitude of the lowest critical load parameters and their corresponding wave numbers ($\hat{n}$) for a wide range of length-to-radius ratios (L/R=2-20) are shown using a solid dark line. It can be seen that most of the lowest critical load parameters occur at $\hat{n}$=2, and that the critical load parameters for the cases of different CNT distributions are FG X-type> UD > FG R-type. The critical load parameters of the cylinder increase when the volume fraction of CNTs becomes greater, which means the cylinder becomes stiffer, while their corresponding wave numbers and the variation patterns between the lowest critical load parameter and length-to-radius ratio will not be affected.

7 Conclusions

On the basis of the RMVT, in this article we have developed the state space DRK method for the 3D buckling analysis of simply-supported, FG CNTRC circular hollow cylinders and laminated composite ones subjected to axial compression. In the illustrative examples, it is shown that these state space DRK solutions of critical load parameters converge rapidly, and are in excellent agreement with the exact 3D solutions and accurate ones obtained using higher-order layerwise theories and ANASYS software for simply-supported laminated composite cylinders available in the literature. When using this method, it is suggested that the highest order of the basis functions (n) should be set at $n \geq$3, the number of uniformly-distributed nodes (N_p) be N_p= 29, and that the radius of the influence zone (a) to be 3.1 times the spacing between the adjacent nodes (i.e., $a = 3.1\Delta z_m$) when n=3 is used. It is also seen in the illustrative examples that the critical load parameters of the cylinders for the cases of different CNT distributions are FG X-type> UD > FG R-type, which reflects the fact that CNT reinforcements that are distributed close to the top and bottom surfaces are more efficient than those distributed near the mid-surface with regard to enhancing the stiffness of the CNTRC cylinders. The critical load

parameters increase when the volume fraction of CNTs becomes greater, while their corresponding wave numbers and the variation between the lowest critical load parameter and length-to-radius ratio will not be affected.

Acknowledgement: This work was supported by the National Science Council of Republic of China through Grant NSC 100-2221-E-006-180-MY3.

References

Anastasiadis, J. S.; Simitses, G. J. (1993): Buckling of pressure-loaded, long, shear deformable, cylindrical laminated shells. *Compos. Struct.*, vol. 23, pp. 221-231.

Anastasiadis, J. S.; Tabiei, A.; Simitses, G. J. (1994): Instability of moderately thick, laminated, cylindrical shells under combined axial compression and pressure. *Compos. Struct*., vol. 27, pp. 367-378.

Atluri, S. N. (2004): *The meshless method (MLPG) for domain & BIE discritizations.* Tech Sci. Press.

Atluri, S. N.; Shen, S. (2002a): *The meshless local Petrov-Galerkin (MLPG) method*. Tech Sci. Press.

Atluri, S. N.; Shen, S. (2002b): The meshless local Petrov-Galerkin (MLPG) method: A simple & less-costly alternative to the finite element and boundary element methods. *CMES: Comput. Model. Eng. Sci.*, vol. 3, pp. 11-51.

Belytschko, T.; Krongauz, Y.; Organ, D.; Fleming, M.; Krysl, P. (1996): Meshless methods: An overview and recent developments. *Comput. Methods Appl. Mech. Eng.*, vol. 139, pp. 3-47.

Carrera, E. (2000a): An assessment of mixed and classical theories on global and local response of multilayered orthotropic plates. *Compos. Struct.*, vol. 50, pp. 183-198.

Carrera, E. (2000b): A priori vs. a posteriori evaluation of transverse stresses in multilayered orthotropic plates. *Compos. Struct.*, vol. 48, pp. 245-260.

Carrera, E. (2003a): Historical review of zig-zag theories for multilayered plates and shells. *Appl. Mech. Rev*., vol. 56, pp. 287-308.

Carrera, E. (2003b): Theories and finite elements for multilayered plates and shells: A unified compact formulation with numerical assessment and benchmarks. *Arch. Comput. Methods Eng.*, vol. 10, pp. 215-296.

Carrera, E.; Brischetto, S. (2009): A survey with numerical assessment of classical and refined theories for the analysis of sandwich plates. *Appl. Mech. Rev*., vol. 62, pp. 1–17.

Carrera, E.; Ciuffreda, A. (2005): A unified formulation to access theories of multilayered plates for various bending problems. *Compos. Struct*., vol. 69, pp. 271-293.

Carrera, E.; Soave, M. (2011): Use of functionally graded material layers in a two-layered pressure vessel. *J. Press. Vessel Tech.*, vol. 133, pp. 1-11.

Chen, S. M.; Wu, C. P.; Wang, Y. M. (2011): A Hermit DRK interpolation-based collocation method for the analysis of Bernoulli-Euler beams and Kirchhoff-Love plates. *Comput. Mech*., vol. 47, pp. 425-453.

Chen, W. Q.; Lü, C. F. (2005): 3D free vibration analysis of cross-ply laminated plates with one pair of opposite edges simply supported. *Compos. Struct.*, vol. 69, pp. 77–87.

Chen, W. Q.; Ding, H. J.; Xu, R. Q. (2001): Three-dimensional static analysis of multilayered piezoelectric hollow spheres via the state space method. *Int. J. Solids Struct*., vol. 38, pp. 4921-4936.

Chou, T. W.; Gao, L.; Thostenson, E. T.; Zhang, Z.; Byun, J. H. (2010): An assessment of the science and technology of carbon nanotube-based fibers and composites. *Compos. Sci. Technol.*, vol. 70, pp. 1-19.

Coleman, J. N.; Khan, U.; Blau, W. J.; Gun'ko, Y. K. (2006): Small but strong: A review of the mechanical properties of carbon nanotube-polymer composites. *Carbon*, vol. 44, pp. 1624-1652.

Donnell, L. H. (1976): *Beams, Plates, and Shells*. McGraw-Hill.

D'Ottavio, M. D.; Carrera, E. (2010): Variable-kinematics approach for linearized buckling analysis of laminated plates and shells. *AIAA J.,* vol. 48, pp. 1987-1996.

Dumir, P. C.; Dube, G. P.; Joshi, S. (2001): Axisymmetric buckling of laminated, moderately thick shallow conical cap. *Arch. Appl. Mech.*, vol. 71, pp. 273-282.

Dumir, P. C.; Dube, G. P.; Mullick, A. (2003): Axisymmetric static and dynamic buckling of laminated thick truncated conical cap. *Int. J. Nonlinear Mech.*, vol. 38, pp. 903-910.

Dumir, P. C.; Dube, G. P.; Mallick, A. (2005): Axisymmetric buckling of laminated thick annular spherical cap. *Commun. Nonlinear Sci. Numer. Simulat.*, vol. 10, pp. 191-204.

Esawi, A. M. K.; Farag, M. M. (2007): Carbon nanotube reinforced composites: Potential and current challenges. *Mater. Des*., vol. 28, pp. 2394-2401.

Hackett, R. M.; Bennett, J. G. (2012): Modeling carbon nanotube reinforced composite materials. *J. Nanomech. Micromech.,* vol. 2, pp. 7-14.

Han, Y.; Elliott, J. (2007): Molecular dynamics simulations of the elastic properties of polymer/carbon nanotube composites. *Comput. Mater. Sci.,* vol. 39, pp. 315-323.

Kardomateas, G. A. (1993): Buckling of thick orthotropic cylindrical shells under external pressure. *J. Appl. Mech.,* vol. 60, pp. 195–202.

Kardomateas, G. A. (1995): Bifurcation of equilibrium in thick orthotropic cylindrical shells under axial compression. *J. Appl. Mech.,* vol. 62, pp. 43-52.

Lei, Z. X.; Liew, K. M.; Yu, J. L. (2013a): Large deflection analysis of functionally graded carbon nanotube-reinforced composite plates by the element-free *kp*-Ritz method. *Comput. Methods Appl. Mech. Engrg.*, vol. 256, pp. 189-199.

Lei, Z. X.; Liew, K. M.; Yu, J. L. (2013b): Buckling analysis of functionally graded carbon nanotube-reinforced composite plates using the element-free. *kp*-Ritz method. Compos. Struct., vol. 98, pp. 60-68.

Li, S.; Liu, W. K. (2002): Meshless particle methods and their applications. *Appl. Mech. Rev.*, vol. 55, pp. 1-34.

Li, S.; Liu, W. K. (2004): *Meshless particle methods*. Springer.

Liew, K. M.; Zhao, X.; Ferreira, A. J. M. (2011): A review of meshless methods for laminated and functionally graded plates and shells. *Compos. Struct.*, vol. 93, pp. 2031-2041.

Liu, G. R.; Gu, Y. T. (2005): *Meshless methods moving beyond the finite element method*. CRC Press.

Lü, C. F.; Chen, W. Q.; Shao, J. W. (2008): Semi-analytical three-dimensional elasticity solutions for generally laminated composite plates. *Eur. J. Mech. A/Solids*, vol. 27, pp. 899-917.

Lü, C. F.; Lim, C. W.; Chen, W. Q. (2009): Semi-analytical analysis for multidirectional functionally graded plates: 3D elasticity solutions. *Int. J. Numer. Methods Eng.*, vol. 79, pp. 25-44.

Noor, A. K.; Burton, W. S. (1990a): Assessment of computational models for multilayered anisotropic plates. *Compos. Struct.*, vol. 14, pp. 233-265.

Noor, A. K.; Burton, W. S. (1990b): Assessment of computational models for multilayered composite shells. *Appl. Mech. Rev.*, vol. 43, pp. 67-97.

Noor, A. K.; Burton, W. S.; Bert, C. W. (1996): Computational model for sandwich panels and shells. *Appl. Mech. Rev.*, vol. 49, pp. 155-199.

Noor, A.K.; Burton, W.S.; Peters, J.M. (1991): Assessment of Computational models for multilayered composite cylinders. *Int. J. Solids Struct.*, vol. 27, pp. 1269-1286.

Noor, A. K.; Peters, J. M. (1989): Stress, vibration, and buckling of multilayered cylinders. J. Struct. Eng., vol. 115, pp. 69-88.

Odegard, G. M.; Gates, T. S.; Nicholson, L. M.; Wise, K. E. (2002): Equivalent-continuum modeling of nano-structured materials. *Compos. Sci. Technol.*, vol. 62, pp. 1869-1880.

Reissner, E. (1984): On a certain mixed variational theory and a proposed application. *Int. J. Numer. Methods Eng.*, vol. 20, pp. 1366-1368.

Reissner, E. (1986): On a mixed variational theorem and on a shear deformable plate theory. *Int. J. Numer. Methods Eng*., vol. 23, pp. 193-198.

Sallam, S.; Simitses, G. J. (1987): Delamination buckling of cylindrical shells under axial compression. *Compos. Struct.*, vol. 7, pp. 83-101.

Saravanos, D. A.; Heyliger, P. R. (1999): Mechanics and computational models for laminated piezoelectric beams, plates, and shells. *Appl. Mech. Rev.*, vol. 52, pp. 305-320.

Shen, H. S. (2001): Buckling and postbuckling of laminated thin cylindrical shells under hygrothermal environments. *Appl. Math. Mech.*, vol. 22, pp. 270-281.

Shen, H. S. (2011a): Postbuckling of nanotube-reinforced composite cylindrical shells in thermal environments, Part I: Axially-loaded shells. *Compos. Struct.*, vol. 93, pp. 2096-2108.

Shen, H. S. (2011b): Postbuckling of nanotube-reinforced composite cylindrical shells in thermal environments, Part II: Pressure-loaded shells. *Compos. Struct.*, vol. 93, pp. 2496-2503.

Shen, H. S. (2012): Thermal buckling and postbuckling behavior of functionally graded carbon nanotube-reinforced composite cylindrical shells. *Compos. Part B: Eng.*, vol. 43, pp. 1030-1038.

Shen, H. S.; Chen, T. Y. (1991): Buckling and postbuckling behavior of cylindrical shells under combined external pressure and axial compression. *Thin-Walled Struct.*, vol. 12, pp. 321-334.

Shen, H. S.; Zhou, P.; Chen, T. Y. (1991): Buckling and postbuckling of stiffened cylindrical shells under axial compression. *Appl. Math. Mech*., vol. 12, pp. 1195-1207.

Sheng, H. Y.; Ye, J. Q. (2002): A state space finite element for laminated composite plates. Comput. Methods Appl. Mech. Eng., vol. 191, pp. 4259-4276.

Sheng, H. Y.; Ye, J. Q. (2003): A three-dimensional state space finite element solution for laminated composite cylindrical shells. *Comput. Methods Appl. Mech. Eng*., vol. 192, pp. 2441-2459.

Simitses, G. J.; Chen, Z. (1988): Buckling of delaminated, long, cylindrical panels under pressure. *Comput. Struct.*, vol. 28, pp. 173-184.

Sladek, J.; Sladek, V.; Solek, P.; Wen, P. H. (2008a): Thermal bending of Reissner-Mindlin plates by the MLPG. *CMES: Comput Model. Eng. Sci.*, vol. 28, pp. 57-76.

Sladek, J.; Sladek, V.; Solek, P.; Wen, P. H. (2008b): Thermal analysis of Reissner-Mindlin shallow shells with FGM properties by the MLPG. *CMES: Comput Model. Eng. Sci.*, vol. 30, pp. 77-97.

Sladek, J.; Sladek, V.; Solek, P. (2009): Elastic analysis in 3D anisotropic functionally graded solids by the MLPG. *CMES: Comput Model. Eng. Sci.*, vol. 43, pp. 223-251.

Sladek, J.; Sladek, V.; Tan, C. L.; Atluri, S. N. (2008): Analysis of transient heat conduction in 3D anisotropic functionally graded solids, by the MLPG method. *CMES: Comput Model. Eng. Sci.*, vol. 32, pp. 161-174.

Soldatos, K. P.; Hadjigeorgiou, V. P. (1990): Three-dimensional solution of the free vibration problem of homogeneous isotropic cylindrical shells and panels. *J. Sound Vib.*, vol. 137, pp. 369-384.

Soldatos, K. P.; Ye, J. Q. (1994): Three-dimensional static, dynamic, thermoelastic and buckling analysis of homogeneous and laminated composite cylinders. *Compos. Struct.*, vol. 29, pp. 131-143.

Wang, Y. M.; Chen, S. M.; Wu, C. P. (2010): A meshless collocation method based on the differential reproducing kernel interpolation. *Comput. Mech.*, vol. 45, pp. 585-606.

Wu, C. P.; Chang, Y. T. (2012): A unified formulation of RMVT-based finite cylindrical layer methods for sandwich circular hollow cylinders with an embedded FGM layer. *Compos. Part B: Eng.*, vol. 43, pp. 3318-3333.

Wu, C. P.; Chen, C. W. (2001a): Elastic buckling of multilayered anisotropic conical shells. *J. Aero. Eng*., vol. 14, pp. 29-36.

Wu, C. P.; Chiu, S. J. (2001b): Thermoelastic buckling of laminated composite conical shells. *J. Therm. Stresses*, vol., 24, pp. 881-901.

Wu, C. P.; Chiu, S. J. (2002): Thermally induced dynamic instability of laminated composite conical shells. *Int. J. Solids Struct.*, vol. 39, pp. 3001-3021.

Wu, C. P.; Jiang, R. Y. (2011): The 3D coupled analysis of FGPM circular hollow sandwich cylinders under thermal loads. *J. Intell. Mater. Sys. Struct.*, vol. 22, pp. 691-712.

Wu, C. P.; Jiang, R. Y. (2012): A state space differential reproducing kernel method for the 3D analysis of FGM sandwich circular hollow cylinders with com-

binations of simply-supported and clamped edges. *Compos. Struct.*, vol. 94, pp. 3401-3420.

Wu, C. P.; Li, H. Y. (2013): RMVT-based finite cylindrical prism methods for multilayered functionally graded circular hollow cylinders with various boundary conditions. *Compos. Struct*., vol. 100, pp. 592-608.

Wu, C. P.; Liu, K. Y. (2007): A state space approach for the analysis of doubly curved functionally graded elastic and piezoelectric shells. *Comput. Mater. Continua*, vol. 6, pp. 177-199.

Wu, C. P.; Chiu, K.H.; Wang, Y.M. (2008): A review on the three-dimensional analytical approaches of multilayered and functionally graded piezoelectric plates and shells. *CMC: Comput. Mater. Continua*, vol. 18, pp. 93-132.

Wu, C. P.; Tsai, T. C. (2012): Exact solutions of functionally graded piezoelectric material sandwich cylinders by a modified Pagano method. *Appl. Math. Modeling*, vol. 36, pp. 1910-1930.

Wu, C. P.; Yang, S. W. (2011a): RMVT-based meshless collocation and element-free Galerkin methods for the approximate 3D analysis of multilayered composite and FGM circular hollow cylinders. *Compos. Part B Eng*., vol. 42, pp. 1683-1700.

Wu, C. P.; Yang, S. W. (2011b): A semi-analytical element-free Galerkin method for the 3D free vibration analysis of multilayered FGM circular hollow cylinders. *J. Intell. Mater. Sys. Struct.*, vol. 22, pp. 1993-2007.

Yang, S. W.; Wang, Y. M.; Wu, C. P.; Hu, H.T. (2010): A meshless collocation method based on the differential kernel approximation. *CMES: Comput. Model. Eng. Sci.*, vol. 60, pp. 1-39.

Ye, J. Q. (2003): *Laminated Composite Plates and Shells-3D Modelling*. Springer.

Ye, J. Q.; Sheng, H. Y. (2003): Free-edge effect in cross-ply laminated hollow cylinders subjected to axisymmetric transverse loads. *Int. J. Mech. Sci*., vol. 45, pp. 1309-1326.

Ye, J. Q.; Sheng, H. Y.; Qin, Q. H. (2004): A state space finite element for laminated composites with free edges and subjected to transverse and in-plane loads. *Comput. Struct.*, vol. 82, pp. 1131-1141.

Ye, J. Q.; Soldatos, K. P. (1994a): Three-dimensional stress analysis of orthotropic and cross-ply laminated hollow cylinders and cylindrical panels. *Comput. Methods Appl. Mech. Eng*., vol. 117, pp. 331-351.

Ye, J. Q.; Soldatos, K. P. (1994b): Three-dimensional vibration of laminated cylinders and cylindrical panels with symmetric or antisymmetric cross-ply lay-up. *Compos. Eng.*, vol. 4, pp. 429-444.

Ye, J. Q.; Soldatos, K. P. (1995): Three-dimensional buckling analysis of laminat-

ed composite hollow cylinders and cylindrical panels. *Int. J. Solids Struct.*, vol. 32, pp. 1949-1962.

Zhang, C. L.; Shen, H. S. (2006): Temperature-dependent elastic properties of single-walled carbon nanotubes: prediction from molecular dynamics simulation. *Appl. Phys. Lett.,* vol. 89, 081904.

Zhao, X.; Liew, K. M. (2011): Free vibration analysis of functionally graded conical shell panels by a meshless method. *Compos. Struct.*, vol. 93, pp. 649-664.

Zhao, X.; Lee, Y. Y.; Liew, K. M. (2009a): Free vibration analysis of functionally graded plates using the element-free *kp*-Ritz method. *J. Sound Vib.*, vol. 93, pp. 649-664.

Zhao, X.; Lee, Y. Y.; Liew, K. M. (2009b): Thermoelastic and vibration analysis of functionally graded cylindrical shells. *Int. J. Mech. Sci.*, vol. 51, pp. 694-707.

Appendix A Derivatives of the DRK interpolation function

Because the DRK interpolation function in the present scheme, $F^a(x,z_m)$, is given in Eq. (49), its first-order derivative with respect to x is thus expressed as

$$\frac{dF^a(x,z_m)}{dx}=\sum_{l=1}^{n_p}\psi_l^{(1)}(x)F_l=\sum_{l=1}^{n_p}\left(\bar{\phi}_l^{(1)}(x)+\frac{d\hat{\phi}_l(x)}{dx}\right)F_l, \tag{A.1}$$

where $\psi_l^{(1)}(x)$ (l=1,2,…, n_p) denote the shape functions of the first-order derivative of $F^a(x,z_m)$ with respect to x, and $\bar{\phi}_l^{(1)}(x)=w_a(x-x_l)\,\mathbf{P}^T(x-x_l)\,\bar{\mathbf{b}}_1(x)$.

The differential reproducing conditions for a set of complete n^{th}-order polynomials are given as

$$\sum_{l=1}^{n_p}\left[\phi_l^{(1)}(x)+\frac{d\hat{\phi}_l(x)}{dx}\right]x_l^r=rx^{r-1}\quad r\le n. \tag{A.2}$$

Equation (A.2) represents (n+1) differential reproducing conditions, and the matrix form of these is given as

$$\begin{aligned}\sum_{l=1}^{n_p}\mathbf{P}(x-x_l)\,\bar{\phi}_l^{(1)}(x)&=\sum_{l=1}^{n_p}\mathbf{P}(x-x_l)w_a(x-x_l)\mathbf{P}^T(x-x_l)\bar{\mathbf{b}}_1(x)\\&=-\mathbf{P}^{(1)}(\mathbf{0})-\sum_{l=1}^{n_p}\mathbf{P}(x-x_l)\frac{d\hat{\phi}_l(x)}{dx},\end{aligned} \tag{A.3}$$

where $(-1)\left[\mathbf{P}^{(1)}(\mathbf{0})\right]=-\left.\frac{d\mathbf{P}(x-x_l)}{dx}\right|_{x=x_l}=\left[\begin{array}{ccccc}0&-1&0&\cdots&0\end{array}\right]^T$.

The undetermined function vector $\bar{\mathbf{b}}_1(x)$ can then be obtained, and this is given by

$$\bar{\mathbf{b}}_1(x) = \mathbf{A}^{-1}(x) \left[-\mathbf{P}^{(1)}(\mathbf{0}) - \sum_{l=1}^{n_p} \mathbf{P}(x-x_l) \frac{d\hat{\phi}_l(x)}{dx} \right]. \tag{A.4}$$

Substituting Eq. (A.4) into Eq. (A.1) yields the shape functions of the first-order derivative of the reproducing kernel interpolation function with respect to x in the form of

$$\psi_l^{(1)}(x) = \bar{\phi}_l^{(1)}(x) + \frac{d\hat{\phi}_l(x)}{dx}, \tag{A.5}$$

where $\bar{\phi}_l^{(1)}(x) = w_a(x-x_l)\mathbf{P}^T(x-x_l)\mathbf{A}^{-1}(x) \left[-\mathbf{P}^{(1)}(\mathbf{0}) - \sum_{l=1}^{n_p} \mathbf{P}(x-x_l) \frac{d\hat{\phi}_l(x)}{dx} \right]$.

Carrying out a similar derivation for the higher-order derivatives of $F^a(x, z_m)$ leads to

$$\frac{d^k F^a(x)}{dx^k} = \sum_{l=1}^{n_p} \psi_l^{(k)}(x) F_l, \tag{A.6}$$

where $\psi_l^{(k)}(x) = \bar{\phi}_l^{(k)}(x) + \frac{d^k\hat{\phi}_l(x)}{dx^k}$,

$$\bar{\phi}_l^{(k)}(x) = w_a(x-x_l)\mathbf{P}^T(x-x_l)\mathbf{A}^{-1}(x) \left[(-1)^k \mathbf{P}^{(k)}(\mathbf{0}) - \sum_{l=1}^{n_p} \mathbf{P}(x-x_l) \frac{d^k\hat{\phi}_l(x)}{dx^k} \right],$$

$$\mathbf{P}^{(k)}(\mathbf{0}) = \left. \frac{d^k \mathbf{P}(x-x_l)}{dx^k} \right|_{x=x_l}.$$